Draft version December 6, 2024
Typeset using LaTeX default style in AASTeX631

Seismic constraints on the spin evolution of slowly rotating young intermediate-mass stars

Kunal H. Singh,[1] Subrata Kumar Panda,[2] Shravan M. Hanasoge,[2] and Siddharth Dhanpal[2]

[1] *St. Xaviers College, Fort, Mumbai 400001, Maharashtra, India*
[2] *Tata Institute of Fundamental Research, Colaba, Mumbai 400005, Maharashtra, India*

ABSTRACT

δ Scuti stars are hot (7000 – 10000K), rapid rotators (10 - 150 $\Omega_\odot$) and are a poorly understood class of pulsators. Asteroseismology provides the only means with which to probe their interior dynamics. However, their complex and unexplained oscillation patterns restrict analyses to only a small fraction with interpretable pulsations. Here, we identify 6711 δ Scutis from 63 sectors of TESS observations, of which 436 had interpretable oscillations, with 38 showing rotational splittings. We inferred compositions and ages (τ) for the 436 stars bf finding them in near-ZAMS states (Bedding et al. 2020), and measured the mean envelope rotation rates ($\langle f_{\rm rot} \rangle$) for the 38 stars. Analyzing their age-dependent rotation, we found these stars essentially exhibit weak-to-no spindown, while evolving past the ZAMS across a narrow time-span during which they show regular pulsations. A quantitative fit to their spin-evolution results in a trend $f_{\rm rot}(d^{-1}) \propto (\tau/{\rm Gyr})^{-0.027\pm0.015}$, much slower than the spindown of cooler late-type stars due to magnetic braking (Skumanich's law, $f_{\rm rot}(d^{-1}) \propto (\tau/{\rm Gyr})^{-0.5}$). Based on MESA calculations, we show this weak spindown is consistent with the gradual increase in their moment-of-inertia.

1. INTRODUCTION

δ Scuti stars are intermediate-mass pulsating stars located near the main sequence and the lower part of the instability strip in the Hertzsprung-Russell (HR) diagram (Uytterhoeven et al. 2011). They are hot stars, with effective temperatures ranging between 5000 K to 10000 K. Their pulsations, primarily driven by the κ-mechanism, (Chevalier 1971), are observed in multiple radial and non-radial acoustic (p) modes and lower radial-order gravity (g) modes (Handler et al. 2009, Guzik 2021). In contrast to the p-mode vibrations of stochastic oscillators (e.g., red-giant and solar-like stars), which are driven by turbulent near-surface convection, the acoustic pulsations in δ Scutis are coherently excited by the opacity-induced κ mechanism in their Helium ionization zones within their stellar envelopes. δ Scuti stars oscillate with relatively high pulsating frequencies, ranging from 5-85 cycles per day ($\rm d^{-1}$). They are also very fast rotators, with surface rotational velocities reaching up to 200 - 300 km/s (Royer, F. et al. 2002).

The fast rotation of δ Scuti stars introduces unusual features such as the extension of the central mixed region (Breger 2000) and complex pulsation patterns. On one hand, the process of deciphering these features grants us a deeper understanding of these stars and the fundamental principles governing them. However, on the other, the very rapid rotation responsible for these distinctive features also presents challenges that impede the thorough study of these stars through asteroseismology. For non-rotating and slowly rotating stars, the pulsation modes may be represented using spherical quantum numbers (n, ℓ, m). Associating these quantum numbers with a particular pulsating mode ('mode identification') is an essential step in constructing accurate models of structure and rotation. However, individual modes of fast rotators, which deform into ellipsoids, cannot be represented with unique sets of (n, ℓ, m) since spherical harmonics are not the correct basis. Linear combinations of spherical quantum numbers can however be used to represent these modes, although this significantly complicates mode identification.

The asymptotic theory of stellar oscillations (Aerts et al. 2010,García & Ballot 2019), of foundational importance in asteroseismology, states that in the regime $n \gg \ell$, p modes of the same degree (ℓ) and successive radial orders (n) are equally spaced in frequency by a separation $\Delta\nu$. This helps in the easy and efficient identification of modes and also provides a foothold for realistic model creation. The pulsation frequencies determined by these models may then be compared with observed frequencies and aid in finding important stellar parameters such as age, mass, composition, etc. Hence, finding stars that display regular frequency spacings helps in shedding light on their internal structure and

dynamics. However, δ Scutis pulsate in low radial-order overtones, i.e., n and ℓ are comparable, and hence may not fall in the asymptotic regime.

However, Reese et al. (2008) showed that for stars rotating at nearly 50% of their Keplerian breakup velocity, 'island modes', which are rotational counterparts of lower-degree modes, show regular frequency spacings in their power spectra, akin to asymptotic theory. Several studies have reported detections of regular frequency separations in δ Scuti oscillation spectra (Matthews 2007, García Hernández et al. 2009, Breger et al. 2011, Zwintz, K. et al. 2011, Paparó, M. et al. 2013, Suárez, J. C. et al. 2014). More recently, Bedding et al. (2020) found 60 δ Scutis which exhibited regular frequency separations in their periodograms from the first 9 sectors of TESS observations. This work motivates our present search, which in addition to providing constraints on the internal structure, allows us to attempt the detection of systematic rotational splittings.

Limitations inherent in ground-based observations of stellar pulsations, such as atmospheric turbulence, light pollution, weather patterns, etc., diminish the quality and continuity of data collection. In this context, the space-based missions CoRoT (Baglin et al. 2009), MOST (Walker et al. 2003; Matthews et al. 2004), Kepler (Borucki et al. 2010) and TESS (Ricker et al. 2015) have played a key role in providing us with high-quality, uninterrupted observations of millions of stars. TESS, a NASA mission, stands as an exemplar of this transformation by capturing high-precision photometric time series from the entire sky. This has in turn yielded a considerably larger dataset for asteroseismic studies compared to previous missions. TESS surveys the sky in small slices, termed sectors. Each sector is of dimension $24^\circ \times 96^\circ$ and it takes TESS approximately 27 days to scan each sector. In the primary mission, TESS surveyed each hemisphere in 13 sectors and subsequently, in their 27-month-long first-extended mission, they again covered both hemispheres over sectors ranging from 27 to 55. The offset in the field of view of the extended mission helps in closing gaps in the sky left during the primary mission. The second-extended mission will focus on the $56^{\rm th}$ to $96^{\rm th}$ sectors.

As reported in Bedding et al. 2020, identifying regularly oscillating δ Scutis is challenging since it involves manually picking candidate stars followed by interactively inspecting their échelle diagrams through a gradual adjustment of $\Delta\nu$. However, owing to the substantially larger data volume than that used by Bedding et al. 2020, extending this approach to stars across 63 sectors poses an algorithmic challenge. To accelerate this discovery process, we developed an 'auto-correlation' method that provides us with a reliable estimate of pulsation regularity and the related $\Delta\nu$.

2. MATERIALS AND METHODS

2.1. *Target selection*

We obtained short-cadence (120 seconds) light-curves for the first 63 sectors of TESS from the MAST database as they are suitable for sampling high-frequency pulsations, such as in δ Scutis. The database comprises 15,000 to 20,000 FITS files of lightcurves captured at 2-minute cadence in each sector. Following the approach laid out in Bedding et al. 2020, we refrain from imposing temperature or luminosity constraints on our sample, and instead focus on using their pulsation characteristics to make the identification. To avoid false positives and misinterpretation of modes, we removed the external sources of periodicity and other object types by taking the steps described in Appendix A and were left with an enormous sample of 292,684 stars.

2.2. *Characterising δ Scutis*

FITS files of light-curves were read using the `lightkurve` (Collaboration & Cardoso 2018) Python package. We then rearranged the light-curves of the same object across different sectors in order of increasing sector number and then unified them using the 'stitch' function from the `lightkurve` package, thereby enhancing the quality of the signal.

Following the criteria outlined in Murphy et al. 2019 and Bedding et al. 2020, we utilized the signal-to-noise ratio (SNR) and skewness to discern between δ and non-δ Scutis.

An initial step involved the computation of the Lomb-Scargle periodograms (Lomb 1976, Scargle 1983) of the light-curves using `lightkurve`. Along the lines of Bedding et al. 2020, we prefer selecting stars with high-frequency pulsations because they are more likely to be pure acoustic modes, and are expected to maintain equal frequency spacing, as dictated by asymptotic theory. In the mid-frequency range, the spectrum is dense, exhibiting a mixed-mode nature due to the proximity of the gravity and acoustic cavities. The low frequency part of the spectrum supports buoyancy modes, and also shows long-period variability such as tidally induced modes, harmonics of rotation frequency, Rossby modes, harmonics of binary-revolution frequencies, motions of surface heterogeneities (e.g., spots), the orbital frequency of the observing satellite, etc. In general, the part of the pulsation spectrum above $5{\rm d}^{-1}$ is considered to fully belong to

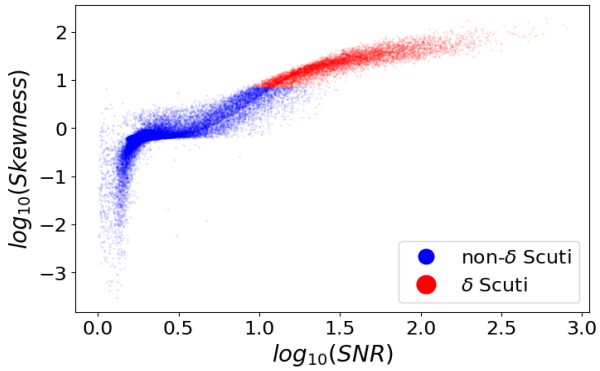

Figure 1: 2D phase-space diagram representing two clusters, δ Scutis (marked in red) and non-δ Scutis (blue).

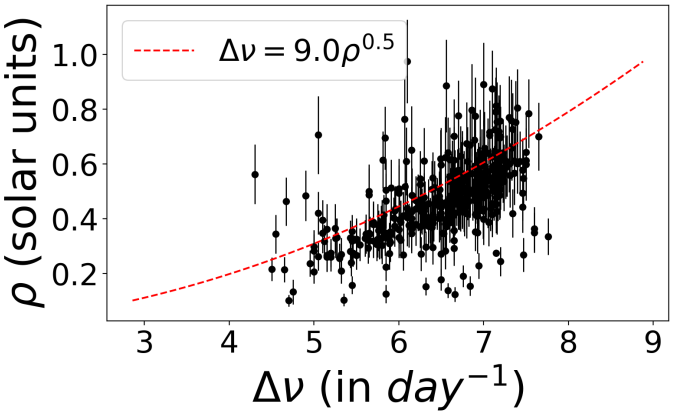

Figure 2: Variation of mean stellar density with respect to large frequency separation ($\Delta\nu$).

the p-mode regime. Therefore, we discard the lower-frequency portions of the power spectra and calculate the SNR and skewness using resonances in the range 30 - 95d^{-1}. The SNR for each star was calculated by dividing the power associated with the highest mode peak by the noise level, where noise corresponds to the 95th percentile of the entire amplitude spectra. Subsequently, we calculated the skewness of each spectrum using readily available routines from SCIPY, distinctly delineating the pulsation peaks from the surrounding background noise. All computations mentioned above were carried out in parallel on a 160-core computing node, making use of the `multiprocessing` (McKerns et al. (2012)) Python package to effectively implement parallelization.

With these computed SNR and skewness values, we constructed a 2D phase-space plot (see Figure 1), which formed two distinct clusters of δ and non-δ Scutis, similar to figure 7 from Murphy et al. 2019.

We then made use of Gaussian Mixture Models (Bishop 2006) using the `scikit-learn` (Pedregosa et al. (2011)) Python package to label the two clusters (figure 1): (i) δ Scuti cluster with high SNR and high skewness, and (ii) non-δ Scuti cluster with low SNR and low skewness. As a result, we were able to identify 6,711 δ Scuti Stars from the first 63 sectors of TESS.

2.3. *Identifying regular pulsations and measurement of* $\Delta\nu$

For a star exhibiting regular frequency pattern, the Échelle diagram with an appropriate value of $\Delta\nu$ will show vertical ridges due to the alignment of modes of identical harmonic degree ℓ (Case A of figure S7). Such an Échelle diagram may be imagined as a matrix with rows of length $\Delta\nu$ and vertical ridges as distinct columns with high-amplitude values (analogous to distinct degrees). Conversely for the same star, but with a $\Delta\nu$ far-off than the appropriate value, we see no such ridge-like structures in the Échelle diagram (case B of figure S7). Finally, for a star that does not has intrinsically regular pulsation pattern (case C of figure S7), the Échelle diagrams will lack aligned ridges regardless of attempting various possible candidate values of $\Delta\nu$.

For a certain Échelle diagram generated assuming a specific $\Delta\nu$, we calculate correlation coefficients between all successive rows and derive a mean of these coefficients, termed 'mean correlation'. We notice that for case A, we will get a higher mean correlation value, while case B results in a lower mean correlation value, even though it is the same star albeit with the wrong $\Delta\nu$ value In contrast, for case C, the mean correlation values remain significantly lower across all the candidate $\Delta\nu$ values. Thus, we deduce that for a regularly pulsating star, if we calculate the mean correlation values for a range of possible candidate $\Delta\nu$ values, then the maxima of all the mean correlation values should correspond to the expected $\Delta\nu$ value. We also find that the stars displaying greater regularity have higher global maxima values, essentially giving us a rough estimate on the extent of regularity of the star (refer supplementary figure S7).

Utilizing this framework, we calculate the mean correlation values across a grid of possible $\Delta\nu$ values in the range 4 to 9 d^{-1} with an interval of 0.002 d^{-1} and find the maximum for each δ Scuti. Using the candidate $\Delta\nu$ value corresponding to the maximum, we construct Échelle diagrams for these stars, as shown in figure S7. We then organize all the stars in descending order of their maximal values. This sorting approach optimizes our examination of regular stars, presenting the 'highly' regular stars upfront and the 'less' regular ones towards the end.

We calculated the uncertainties for $\Delta\nu$ by fitting a Lorentzian to the highest peaks of the correlation function of each star. The centers of the Lorentzian peak are selected as the reported $\Delta\nu$ values and half of the Lorentzian width is considered as the uncertainty. The Lorentzian function is defined according to equation 1,

$$\frac{A}{\pi}\left(\frac{\frac{\Gamma^2}{4}}{(x-x_0)^2+(\frac{\Gamma}{2})^2}\right), \tag{1}$$

where A is the amplitude of the Lorentzian peak and Γ is the Full Width Half Maximum.

Employing this method, we successfully identified 436 δ Scutis displaying regular frequency separations from a total sample of 6,711 δ Scutis. This approach significantly reduced the time and effort in this process. We show the Échelle diagrams of several δ Scuti stars in figure S3 that exhibit regular pulsations. Parts of the spectra appear clearer in the higher-frequency range, and turn fuzzier at the lower end, where various signals contribute to variability, as discussed in section 2.2. Multiple ridges are observed in some Échelle diagrams, which may be attributed to signatures arising from higher-degree modes (e.g., $\ell = 2, 3$), as suggested in Bedding et al. 2020.

Figure 2 demonstrates that the computed $\Delta\nu$ for the stars showing regular pulsation closely follows the standard scaling relation $\Delta\nu \propto \rho^{0.5}$ (Ulrich (1986)), where mean stellar density(ρ) is obtained from TESS Input Catalogue hosted at the vizier database(Ochsenbein et al. 2000). The large-frequency separations ($\Delta\nu$) of the 436 stars show an asymmetric distribution (figure S1) skewed towards a higher value, representing an enhanced population of relatively young stars in our samples, as $\Delta\nu$ is known to gradually decrease with stellar evolution. This implication is in agreement with the observed over-abundance of young stars, shown further in figure 3(c).

By identifying the $\Delta\nu$ of regularly oscillating δ Scutis, our study can effectively constrain stellar physical parameters such as mean stellar density, mass, radius, etc. We find that 6% of all the δ Scutis discovered show regular frequency separations in their oscillation spectra, which is consistent with the findings reported in Bedding et al. 2020. Given the large dataset we worked with, this analysis can help us gain a detailed understanding of the different stages of δ Scuti stars' evolution. The question of why only 6% of δ Scutis pulsate in a regular manner remains. All the 6,711 δ Scutis in our sample and the 436 that show equally spaced acoustic mode patterns are homogeneously distributed across the sky (figure S2), which rules out specific regions of the galaxy preferentially harboring these stars. However, the 436 regular pulsators lie tightly clustered around the ZAMS line in the HR diagram (figure S4), whereas the rest uniformly cover the main-sequence region. This suggests that stars showing regular pulsation patterns are indeed near-ZAMS stars, as also argued by Bedding et al. 2020. Since such young stars possess pulsation cavities that are simpler in structure (Handler et al. 2009), they may be vibrating with purely acoustic modes, thus resulting in a cleaner spectra with equally spaced frequencies. As Handler et al. (2009) has suggested, with gradual main-sequence evolution, mixed modes start entering the spectrum, possibly leading to the dense appearance of δ Scuti spectra.

2.4. *Fitting stellar models*

We attempt to infer the internal structure of these stars in an effort to appreciate features that drive their regular oscillations. Deploying a modified version of the conventional χ^2 minimization between the spectroscopic-asteroseismic observations and the stellar-model grid available from Murphy et al. (2023), we intended to obtain the best-fit models (M, Z, τ) for each of the 436 stars identified in Section 2.3. The model grid (Murphy et al. 2023) comprises over 200,000

stellar models covering a wide range over mass, metallicity, and age. This grid also provides pulsation frequencies of radial and dipole zonal modes with frequencies up to $95 \mathrm{d}^{-1}$. For easier comparison against real spectra, we developed power spectra by constructing sinc profiles (Dupret, M.-A. et al. 2009; Ziaali et al. 2019; Barac et al. 2022) of identical amplitudes around each of these eigenfrequencies. Although it does not exactly model the amplitude structure in the observations, it serves the purpose of frequency-profile matching between models and observations. The amplitude scale is not a concern because we normalize both spectra to allow for direct comparison.

Although rotation has not been implemented in this stellar model grid, it has been used by various authors (Murphy et al. 2020, 2021, 2022; Scutt et al. 2023) to model slow-to-intermediate rotating δ Scuti stars. The grid incorporates convective overshooting using an exponentially decaying mixing scheme (Murphy et al. 2023) implemented at the boundaries of convective cores and at the surface layers.

In several contexts, many authors (Reeth et al. 2015; Bazot, M. et al. 2019; Murphy et al. 2021; Steindl, T. et al. 2022) have used χ^2 minimization techniques to fit relevant parameters to astrophysical observations, including multiple asteroseismic oscillation frequencies. In this method, χ^2 denotes the differences between model and observation and samples with $\chi^2 \leq 1$ are considered good models. The median and variance of the parameters corresponding to these good models are treated as the uncertainties associated with the best-fit solution. The asteroseismic term in the χ^2 expression compares the oscillation frequencies of observations and the model possessing the same mode characteristics, thereby making prior mode identification a necessary requirement. Therefore, it is only applicable when modes can be unambiguously characterized, limiting the applicability of this strategy to only a few stars. Thus, manual investigation of mode identities makes it difficult to automate this method to address a larger sample of stars. Left with the challenge of modeling 436 stars lacking proper mode labels, we resorted to adopting a modified version of χ^2 minimization as we elaborate below.

Our merit function involves model-observation comparisons over two categories of terms, first, the comparison of $(L,\ T_{\rm eff},\ \Delta\nu)$ and second, the similarity between the modeled and the observed spectra. Different stars are observed for different temporal durations ($T_{\rm obs}$) and therefore the spectral resolution ($1/T_{\rm obs}$) varies across the sample. For a minimum one sector of observation, TESS data allows a resolution of $0.037\ \mathrm{d}^{-1}$. However, we need a common frequency resolution for all the stellar spectra in our sample since they need to be compared with thousands of model spectra having identical resolution. Thus, after computing the individual power spectra, we interpolated all of them on to a frequency grid spanning $1 - 95\ \mathrm{d}^{-1}$ comprising 10000 array elements (resolution of $\sim 0.0094\ \mathrm{d}^{-1}$). Choosing a frequency grid of still higher resolution will increase the computational cost without significantly impacting the inference. However, adopting a coarser resolution may result in important pulsation modes being neglected, leading to mis-identifications of best-fit solutions. Given a stellar observation characterized by $(L_\star,\ T_{\rm eff\star},\ \Delta\nu_\star,\ \mathrm{spectra}_\star)$, the stellar model represented by $(L_{\rm model}, T_{\rm eff;model},\ \Delta\nu_{\rm model}, \mathrm{spectra}_{\rm model})$ is compared according to the following merit function

$$\chi^2_{\star,\rm model} = (L_\star - L_{\rm model})^2 + (T_\star - T_{\rm model})^2 + (\Delta\nu_\star - \Delta\nu_{\rm model})^2 + \left(\frac{1}{\mathrm{spectra}_\star \otimes \mathrm{spectra}_{\rm model}}\right)^2,$$

where '$\otimes$' represents the summed-correlation (or equivalently the 'dot product'), which is a scalar value obtained by adding the element-wise products of two arrays. To avoid the dot product yielding very large values in the last term, we normalized each spectra ($\mathrm{spectra}_\star \rightarrow \mathrm{spectra}_\star/\sqrt{\mathrm{spectra}_\star \otimes \mathrm{spectra}_\star}$; $\mathrm{spectra}_{\rm model} \rightarrow \mathrm{spectra}_{\rm model}/\sqrt{\mathrm{spectra}_{\rm model} \otimes \mathrm{spectra}_{\rm model}}$). Hence, the correlation term $\mathrm{spectra}_\star \otimes \mathrm{spectra}_{\rm model}$ is constrained so as to never exceed unity. The model with the lowest $\chi^2_{\star,\rm model}$ value may be considered the best fit, which happens when $(L_{\rm model}, T_{\rm eff;model},\ \Delta\nu_{\rm model})$ are closest to $(L_\star,\ T_{\rm eff\star},\ \Delta\nu_\star)$ and the correlation term $\mathrm{spectra}_\star \otimes \mathrm{spectra}_{\rm model}$ is closest to unity.

To find the best model across the entire grid for a given star, one would need to compute the $\chi^2_{\star,\rm model}$ for all model samples and subsequently identify the set of parameters for which this assumes the lowest value. The four individual terms in the $\chi^2_{\star,\rm model}$ can vary over distinct scales (e.g., $\sim 10^{-2} L_\odot^2,\ \sim 10^4 K^2,\ \sim 10^{-2}\mathrm{d}^{-2}$), with $T_{\rm eff}$ dominating the other components. The appropriate weighting of each of these terms is important to generating accurate best-fit models. We might have scaled the first three difference terms by their 1σ uncertainties but the final correlation term does not show well defined uncertainty. Trial and error led us to better solutions when each term is separately normalized by its corresponding largest value across the entire model grid. This ensures that each term in the $\chi^2_{\star,\rm model}$ stays between 0 and 1 regardless of the model and star. Equation 2 expresses these ideas in a mathematical form, with the symbol '$\mathcal{N}$' representing normalization across the entire grid.

$$\chi^2_{\star,\mathrm{model}} = \mathcal{N}\left\{(L_\star - L_{\mathrm{model}})^2\right\} + \mathcal{N}\left\{(T_{\mathrm{eff};\star} - T_{\mathrm{eff;model}})^2\right\} + \mathcal{N}\left\{(\Delta\nu_\star - \Delta\nu_{\mathrm{model}})^2\right\} + \mathcal{N}\left\{(\mathrm{spectra}_\star \otimes \mathrm{spectra}_{\mathrm{model}})^{-2}\right\} \quad (2)$$

This may be more clearly seen when the equation 2 is rephrased as

$$\chi^2_{\star,\mathrm{model}} = \frac{(L_\star - L_{\mathrm{model}})^2}{\max\limits_{\text{all models}}[(L_\star - L_{\mathrm{model}})^2]} + \frac{(T_{\mathrm{eff};\star} - T_{\mathrm{eff;model}})^2}{\max\limits_{\text{all models}}[(T_{\mathrm{eff};\star} - T_{\mathrm{eff;model}})^2]} + \frac{(\Delta\nu_\star - \Delta\nu_{\mathrm{model}})^2}{\max\limits_{\text{all models}}[(\Delta\nu_\star - \Delta\nu_{\mathrm{model}})^2]} + \frac{(\mathrm{spectra}_\star \otimes \mathrm{spectra}_{\mathrm{model}})^{-2}}{\max\limits_{\text{all models}}[(\mathrm{spectra}_\star \otimes \mathrm{spectra}_{\mathrm{model}})^{-2}]}$$

We prefer the inclusion of the spectral-correlation term in the χ^2 metric over the commonly used eigenfrequency-comparison, especially because of ambiguities in assigning labels to observed oscillation modes. A similar spectral correlation technique was also used by Li et al. (2022) for parameter-fitting to Kepler RGB stars.

With this setup, the best-fit model will have a very small $\chi^2_{\star,\mathrm{model}}$ and the model that maximally differs from observation will possess a $\chi^2_{\star,\mathrm{model}}$ around 4. For a particular star, the $\chi^2_{\star,\mathrm{model}}$ values obtained for all models leads to a Gaussian dip in the vicinity of the global minimum (similar to Fig. 9 of Murphy et al. 2021 in the 3D phase space of (M, Z, τ)). We computed the best-fit solutions by identifying the model associated with the lowest merit function, and obtained corresponding uncertainties by calculating the $1-\sigma$ parameter spread of neighbouring models whose merit functions stay below unity. While calculating the expected values and uncertainties, we did not disentangle the three structure parameters, rather treating them as a single entity to retain their mutual correlations intact.

Equation 2 effectively contrasts all four aspects of the model against observations. Therefore, we were able to obtain convincing fits to the examined stars. The χ^2_{min} values of all the stars we analyzed are available in the supplementary Table S1. We utilized the `stats` module of the Python package `Scipy` to calculate the statistical significance of our best-fit models using the function `chi2`. This function requires two input arguments – χ^2_{min} and degree of freedom (df) to compute the significance level by obtaining the desired area below the χ^2 distribution function $f(\chi; df)$. Since we fit 4 independent stellar observations ($L, T_{\mathrm{eff}}, \Delta\nu$, spectra) with 3 free parameters (M, Z, τ), the effective degree of freedom in our case is 1. For all the stars we analyzed, statistical significance lies between 70% and 96% (Figure S10), with 412 of them possessing above 80% significance. In Table S1 and the supplementary resource we provide the statistical significance of all stars.

Finally, rotational mixing within the radiative envelopes, which is not incorporated in stellar evolution models, might play a significant role in perturbing the structure and pulsations of intermediate-mass main-sequence stars (Pedersen 2022a). Hence, our reported best models based on χ^2_{min} may not accurately capture all relevant aspects of stellar structure. Within our present capabilities, they offer the best potential representations to the overall observations of these targets.

Figure 3 indicates that, while mass and metallicity tend to cluster around $1.6 M_\odot$ and 1% (or [Fe/H] ~ -0.146) respectively, the age distribution is bimodal. Most stars appear to have low metallicity as compared to the Sun, i.e., $Z_\odot = 0.019$. The [Fe/H] values for these stars as obtained from Gaia DR3 (Gaia Collaboration et. al. 2018) also support this assertion (figure S6). Bimodality in age may arise from the fact that δ Scuti-like oscillations are often excited across a diverse evolutionary phases – ranging from pre-main sequence to the terminal age main sequence, and occasionally even beyond. Some δ Scutis exhibit comparable asteroseismic structure parameters through these different evolutionary phases, which may cause degeneracy in age determination, especially because we only have access to a limited number of observables. The left peak in the age-distribution figure may be pointing to the pre-main phase stars and the right, to those in the main sequence proper. However, most stars were found to be younger than 30 Myr, consistent with Bedding et al. (2020), suggesting that stars with regular patterns are likely in near-ZAMS phases.

The convective cores of δ Scuti stars play an important role in their evolution, as they generate the entire energy necessary to counteract the gravitational collapse. We evolved all 436 regularly pulsating stars using their best fit parameters and determined the mass of their convective cores. We show its distribution and age-dependence in figure S8.

These inferences also possess the potential to help in characterizing open clusters in which δ Scutis may be present, allowing for constraining the related parameters (Handler et al. 2009). Recently, Bedding et al. (2023) identified the

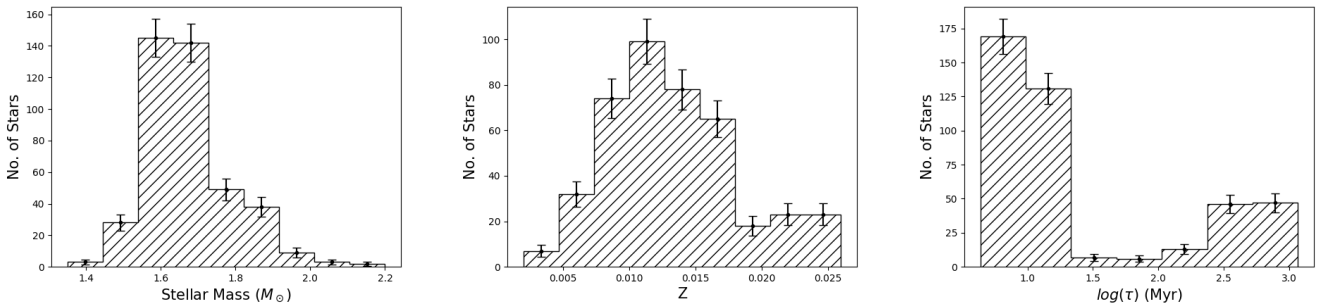

(a) (b) (c)

Figure 3: Distributions of stellar parameters M, Z, and $\log(\tau/\mathrm{Myr})$, obtained from fitting models to spectroscopic and seismic observations of 436 regular oscillators.

presence of several δ Scutis in TESS observations of the Pleiades cluster, underscoring a promising avenue for future investigations.

3. RESULTS AND DISCUSSION

Stellar rotation is very important in inferring age and magnetism and plays a crucial role in influencing stellar structure (Vidotto et al. 2014). Asteroseismology has been highly successful in measuring the internal rotation rates of various pulsating stars. Because of the number of orderly asymptotic modes with accurately labelled rotational splittings, rotation inferences of red giants (Deheuvels et al. 2012) and solar-like oscillators (Benomar et al. 2015) has met with success. Asteroseismologists are able to place constraints on their radial and latitudinal differential rotation rates (Bazot, M. et al. 2019; Benomar et al. 2018). Owing to their gravity-mode pulsations, whose mode identifications have recently become possible with high-resolution spectra from Kepler, notable progress has been made in inferring the rotation rates of rapidly spinning hot main-sequence stars, which include intermediate-mass γ Doradus (Reeth et al. 2015), high-mass slowly pulsating B stars (Pedersen 2022b) and β Cepheids (Pamyatnykh et al. 2004; Briquet et al. 2007; Suárez et al. 2008; Bowman 2020). This has generated several new insights, including cores rotating much faster than envelopes (Deheuvels et al. 2012), envelopes rotating slightly faster than cores (Kurtz et al. 2014), and cores slowing down with stellar age (Pedersen 2022b).

However, the identification of rotational multiplets in δ Scutis has long remained a formidable problem. Obstacles to this goal are (i) intrinsic amplitude suppression of certain multiplets, (ii) lower inclination angles, favouring zonal modes, or (iii) large ($\mathrm{f_{rot}} \sim \Delta\nu$) asymmetric splitting of multiplets, disrupting traditional structure in spectra. While the first scenario has been explicitly observed in γ Doradus stars as prograde mode excitation (Li et al. 2019), the second may be justifiable for δ Scutis showing regular patterns, and the last point seems applicable to rapid rotators. Some of the success down this line includes, but is not limited to, the discovery of a dipole triplet in V 624 τ (Fox Machado, L. et al. 2006), spectroscopic identification of rotational splits in FG Vir (Zima, W. et al. 2006), observation of rotational multiplets in 31 CoRoT δ Scutis (Paparó et al. 2016), and detection of four dipole doublets in HD 23642 (Southworth et al. 2023) among others. However, simultaneous measurements of rotation and age on a larger sample are still lacking - which we are attempting to carry out in this work. Our present sample is limited to slow rotators in a short near-ZAMS phase of evolution, and hence is not representative of the entire class of δ Scuti stars.

3.1. *Discerning rotational splittings in δ Scuti stars*

We investigated rotational splitting patterns exhibited by (dominantly) dipole modes in a selected group of 38 stars. This set was manually chosen by identifying spectra in which multiplet-like structure was seen across at least two radial orders of dipole modes. We show Échelle diagrams of two different stars in figure S5, where rotational splittings are observed across several radial orders, thus supporting the idea that they are multiplets arising from rotational perturbations. The doublet patterns seen in the Échelle diagrams are presumed to be $m = -1$ and $m = +1$ modes – which, invoking traditional seismic interpretation, offer an avenue to infer the rotation rate.

Rotational splittings in δ Scuti stars can take on unexpected and complicated forms. For instance, it has been argued that prograde ($m = +1$) modes are selectively driven (Reeth et al. 2015) in γ Doradus stars. Similarly, δ Scutis

also show peculiar rotational splittings, e.g., Southworth et al. (2023) has observed dipole splittings at radial order $n = 1, 2, 3, 6$ with $m = 0$ modes consistently absent (see their Figure 4 and 3) in all harmonics in the binary star HD 23642 (only $m = \pm 1$). Based on this, they conclude that the star is seen nearly edge-on. They determined the rotation frequency to be half the doublet spacing, which is also consistent with the synchronized binary orbital period of this system. In the 38 stars we examined, we noticed identical dipole doublet features in the Échelle diagrams of 24 stars, with the exception of $m = 0$ modes occasionally showing up at certain radial orders in the remaining 14 stars. Therefore, along similar lines of argument, we assume that wherever we observe doublets, they may be identified as $m = \pm 1$.

Stars are likely to not rotate as rigid bodies. They exhibit radially as well as latitudinally varying rates of rotation, although the extent differs among different categories of stars. The rotational splittings observed in oscillation spectra are a consequence of the sum of internal rotation profiles weighted by the mode sensitivity. Only in the case of uniformly rotating stars is the mode splitting a direct measure of the rotation rate of the star. Although differential rotation has been well constrained in solar-like stars (Benomar et al. 2018), little is known about this phenomenon in δ Scutis. Kurtz et al. (2014) estimated that main-sequence δ Scuti KIC 11145123 exhibited rigid rotation, with the envelope spinning only 3% faster than the core. Schmid, V. S. et al. (2015) reported KIC 10080943 as an eccentric binary system with both the primary and secondary components comprising morphologically similar δ Scuti - γ Doradus hybrids, in which they observed the envelope to rotate 1% slower (3% faster) than the core in the primary (secondary) component. Murphy et al. (2016) concluded that main-sequence star KIC 7661054 rotates approximately uniformly, with its surface rotating slightly faster than its core. Based on these lines of argument, we invoke the assumption of rigid body rotation for the stars we analyzed. Since we use the splittings of low-radial order p-modes (confirmed by matching with the best-fit model's pulsation), whose sensitivities peak in the outer layers, our measurements are likely indicative of near-surface (or outer envelope) rotation. Even in the presence of differential rotation within the outer stellar layers, our reported values may be considered to be the average envelope rotation.

When accounting for only the effect of Corilois force and ignoring centrifugal deformation for a differentially rotating star, the frequencies of rotationally perturbed oscillation modes in the observer's frame may be written as (Kurtz et al. 2014)

$$\nu_{\rm inertial} = \nu_{\rm co-rotating} + m(1 - C_L) \int_0^R K_{n,\ell}(r) f_{\rm rot}(r) dr,$$

where

$$C_L = \frac{\int_0^R \xi_h (2\xi_r + \xi_h) r^2 \rho dr}{\int_0^R [\xi_r^2 + \ell(\ell+1)\xi_h^2] r^2 \rho dr}$$

is the Ledoux constant (Ledoux 1951), and

$$K_{n,\ell} = \frac{[\xi_r^2 + \ell(\ell+1)\xi_h^2 - 2\xi_r\xi_h - \xi_h^2]\rho r^2}{\int_0^R [\xi_r^2 + \ell(\ell+1)\xi_h^2 - 2\xi_r\xi_h - \xi_h^2]\rho r^2 dr}$$

is a weight factor known as the rotation kernel, which captures mode sensitivity as a function of stellar radius. ξ_h and ξ_r denote the horizontal and radial displacements of the mode eigenfunction, computed with respect to the equilibrium configuration.

The rotation kernels for p-modes are more sensitive to the outer stellar layers (Fig. 12 of Kurtz et al. 2014). With increasing radial order, their probing power shifts ever more towards the surface. Hence, denoting the average near-surface envelope rotation as $\langle f_{\rm rot} \rangle$, rotationally split frequencies may be written as

$$\nu_{\rm in.} = \nu_{\rm co.} + m(1 - C_L)\langle f_{\rm rot} \rangle.$$

Due to the moderate-to-fast rotation, second-order perturbation theory may be required in order to explain the rotational frequency splittings of δ Scuti stars (Suárez, J. C. et al. 2006). This includes the effect of centrifugal deformation on mode frequencies, which also shifts the $m = 0$ component, causing the frequency spacing to become asymmetric. This is why the $m = 0$ component does not appear for some spectra at the midpoint between the $m = \pm 1$ doublet. Combining both first- and second-order effects, the frequencies as measured in the inertial frame may be written as

$$\nu_{n,\ell,m} = \nu_{n,\ell} + m(1 - C_L)\,\langle f_{\rm rot} \rangle + (D_0 + m^2 D_1) \frac{\langle f_{\rm rot} \rangle^2}{\nu_{n,\ell}},$$

where the coefficients $\{D_0, D_1\}$ represent complicated functions of stellar structure and displacement eigenfunctions (Suárez, J. C. et al. 2006).

As shown below, the average envelope rotation $\langle f_{\rm rot}\rangle$ may be inferred from the sectoral dipole multiplets ($m = \pm 1$), without requiring asymmetry coefficients or the $m = 0$ frequencies.

$$\nu_{n,1,1} - \nu_{n,1,-1} = 2(1 - C_L)\langle f_{\rm rot}\rangle.$$

Hence, we use equation 3 to calculate the average envelope rotation, which use the dipole doublets seen in the 38 stars. Similar formulae have been theoretically and numerically (Reese, D. R. et al. 2009; Deupree 2011) established as valid, even for cases with rapid rotation and asymmetric splitting. The Ledoux constant for p-modes often assumes very small values, e.g., 0.03 for the stellar model of KIC 11145123 (Kurtz et al. 2014), and not larger than 0.02 for the 38 stars we studied.

$$\langle f_{\rm rot}\rangle = \frac{\nu_{m=+1} - \nu_{m=-1}}{2(1 - C_L)} \tag{3}$$

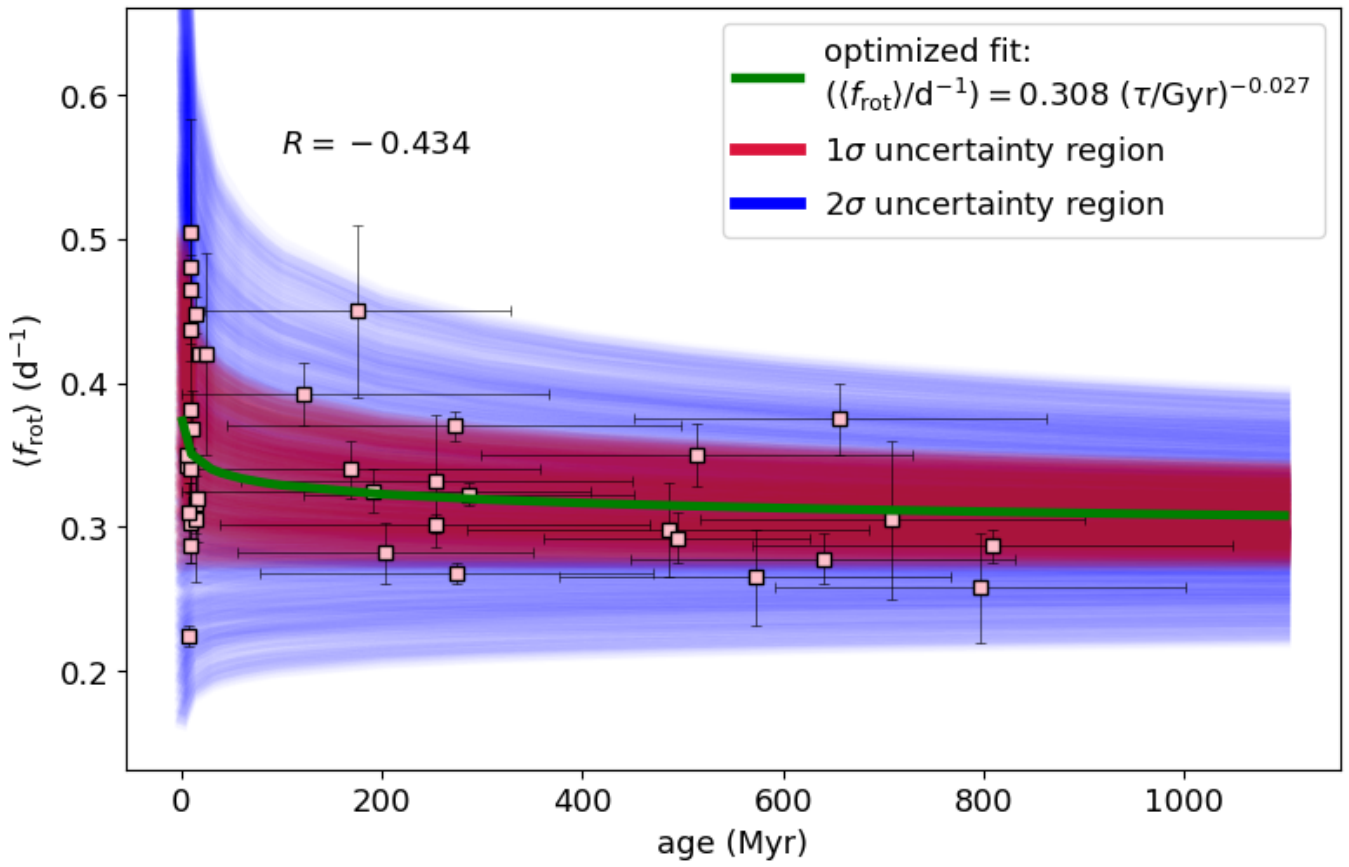

Figure 4: Evolution of average envelope rotation with age of slow-rotating near-ZAMS δ Scuti stars. These stars, *covering a tiny phase space of the rotation-age landscape*, show weak-to-no spin down. The Pearson correlation coefficient for the dependence between $\langle f_{\rm rot}\rangle$ and age yields $R = -0.434$. Similar analysis results in a correlation of $R = -0.379$ between $\log\tau$ and $\log f_{\rm rot}$. Larger rotation spread for the youngest stars further reduces the expected correlation. The green line shows the best-fit curve to the data, which appears to follow a $\langle f_{\rm rot}\rangle \propto (\tau/{\rm Gyr})^{-0.027\pm0.015}$ trend, with $f_{\rm rot}$ measured in d^{-1}. The 1- and 2-σ uncertainty regions are shown as solid patches by plotting the characteristic functions with parameters sampled within the 1σ or 2σ uncertainty ellipses centered at the best fit values.

3.2. *Gyrochronological Implications*

Late-type stars generate a strong magnetic field due to the motion of the ions in their convective zone, which acts as a dynamo. With increasing age, stellar angular momentum decreases as the magnetic field causes ionized wind to blow outward, in turn leading to a decrease in their rotation rate - termed magnetic braking. Stars with higher rotation rates have stronger magnetic fields (Soderblom & Valenti (2007)), thereby leading to a more rapid spindown. This feedback mechanism leads to the convergence of rotation rates over time, and they eventually follow the Skumanich spin down law, $f_{\rm rot} \propto t^{-0.5}$ (Skumanich (1972)). This phenomenon has been consistently studied in open clusters of ages 100-650 Myr, Hyades (650 Myr, Radick et al. 1987), Pleiades (500 Myr, Barnes 2007), Coma Berenices(650 Myr, Collier Cameron et al. 2009), M37 (550 Myr, Hartman et al. (2009). This limitation is a big hurdle as clusters of age $\sim$ 500 Myr are quite rare. The spindown relation is also useful in inferring ages for field stars as shown by various studies (Mamajek & Hillenbrand 2008, Meibom et al. 2009, McQuillan et al. 2014, and Reinhold, Timo & Gizon, Laurent 2015). The method of determining stellar ages from rotation rates is termed Gyrochronology (Barnes 2003). Asteroseismology, which can be applied to measure stellar rotation, assists typically in accurately constraining ages of cool stars.

We investigated how rotation rates correlate with their ages for this ensemble.

We show the age dependence of the mean envelope rotation rates of our sample in figure 4. This sample is limited to slowly rotating stars in the near-ZAMS phase and hence does not capture the complete landscape of rotation rates or spin evolution of the full δ Scuti class. While slowly rotating stars make it easier to discern rotational splitting, near-ZAMS δ Scutis allow for seismologically constraining their ages through the regular oscillation pattern they exhibit.

We fit a power-law function of form $\langle f_{\rm rot} \rangle (\mathrm{d}^{-1}) = \alpha(\tau/\mathrm{Gyr})^{\beta}$ to the age-rotation characteristics shown in Figure 4. Since both uncertainties in ages and rotations are non-negligible, we adopted an error-in-variables approach to fit the data. Specifically we used the orthogonal distance regression (ODR) algorithm available in the Python package `Scipy` which implements the FORTRAN routine `ODRPACK` to minimize the perpendicular distance between observed data points and the test function. This approach is superior in the present case since it accounts for uncertainties in both the ages inferred and rotation rates. ODR fits our inferences with $\{\alpha = 0.308 \pm 0.018, \beta = -0.027 \pm 0.015\}$. The algorithm moreover provides the covariance matrix whose eigenvalues and eigenvectors represent the squared-length and directions of the principal axes of 1σ error ellipse (or, 68% confidence interval). For the $2-\sigma$ error ellipse (95% confidence interval), the principal axes scale by $\sqrt{5.991}$ in magnitude. Subtracting the best fit solution from the observation data, the algorithm provides a reduced residual $\chi^2 = 0.241$ (d^{-1}), with a statistical significance of 88%. Figure 4 conveys that the stars in our sample do not show significant spin-down, decidedly weaker than that for cool stars.

δ Scutis are A-F type (7000 - 10000K surface temperature) stars and their large radiative envelopes or the tiny convective cores are unlikely to create strong dynamo magnetic fields. Consequently, magnetic braking may not play an important role in spindown (Neiner & Lampens 2015; Ahlers et al. 2019), and there is thus a need for an alternate theoretical framework. A small fraction ($\sim$10%) of hot stars are known to possess strong magnetic fields (Braithwaite & Spruit (2004)), called fossil magnetic fields, which are remnants of magnetic field from the protostellar clouds and are usually dipolar in morphology. Such fields, which have been observed in δ Scutis (Neiner et al. (2017); Neiner & Lampens (2015)), have the capacity to permeate the entire star and subsequently transfer angular momentum (AM) to deeper layers, resulting in an effective loss of AM (Keszthelyi et al. 2020). These field configurations in hot stars causes them to rotate slower than in a purely hydrodynamic setting. β Cas (Zwintz et al. (2020)) is the only known δ Scuti to show the presence of a dynamo magnetic field. It is possible that fossil magnetic fields transition to dynamo fields as the star evolves. Unrelated mechanisms such as disk accretion (Amard & Matt 2023) may also be at play.

Internal gravity waves can also drive AM transport in stars with convective cores and radiative envelopes, including δ Scutis and B-type stars (Fuller et al. 2014; Rogers 2015). These waves transport AM from the location at which they are excited (core-envelope interface) to the convectively stable dense envelope, where they undergo dissipation and deposit AM. Due to its stochastic nature, this mechanism can alternately increase or reduce the envelope rotation rate (Rogers 2015). The dynamics are inherently two-dimensional and cannot be simulated in 1D stellar models such as the ones we consider here. Internal gravity waves may be inducing the rotational decay we report in this study although more detailed calculations are required to quantify their role.

Over their evolution through the main sequence, stars swell in size, and their momenta of inertia ($I(\tau) = 4\pi \int_0^{R_\star(\tau)} \rho(r,\tau) r^4 \, dr$) systematically increases. Assuming rigid body rotation and conservation of AM (L_0) throughout

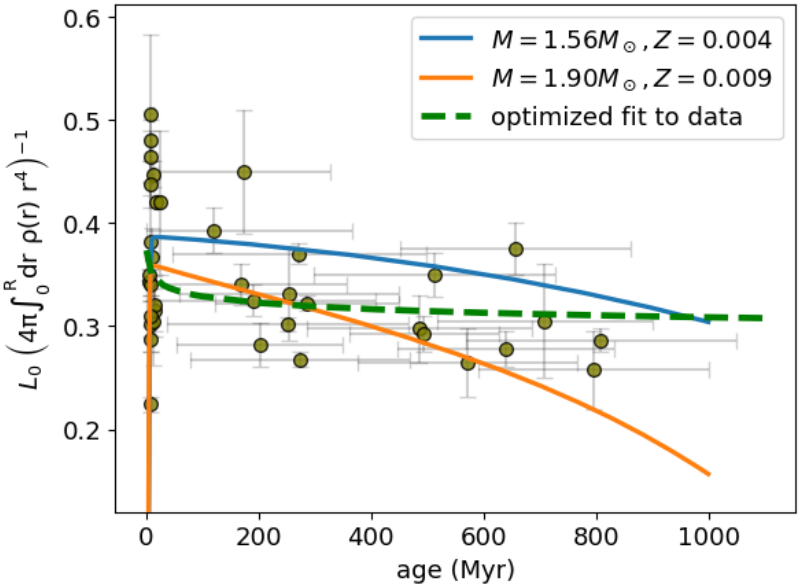

Figure 5: Age-dependent variation of the inverse moment of inertia ($I^{-1}(t)$) of two stars of different masses, scaled by arbitrarily assumed initial AM $L_0 = 0.4$ and 0.6 $M_\odot R_\odot^2 d^{-1}$ for stars of masses $1.56 M_\odot$ and $1.90 M_\odot$ respectively. In early phases, stars pass through the pre-main sequence phase of rapid contraction, which reduces their moment of inertia and causes a sharp rise in the rotation rate. During the main sequence this quantity gradually drops as a consequence of the rising momentum of inertia resulting from the radial expansion of these stars. In the background, we plot the rotation rates of the observed stars (figure 4) and the best fit model for direct comparison.

the evolution, the rotation rate ($\Omega(\tau) = L_0/I(\tau)$) is expected to decay with stellar age, commensurate with $I^{-1}(\tau)$. Below, in figure 5, we show how the inverse moment of inertia of two different stars, scaled by arbitrary initial AM (L_0), vary as function of age. This explanation is able to describe the observed weak-to-no spindown.

It is more informative to study the spin evolution of stars with their evolutionary states. Core Hydrogen content is one of the direct indicators of stellar evolution as it provides the fuel budget necessary to support various dynamics of the stars. We evolved the 38 stars, that show rotational splittings, using their best fit structures and obtained their core Hydrogen abundances. We show in figure S9 the dependence of average stellar rotation with the core Hydrogen content and the evolution of the latter with the stellar ages. Finally, as an aside, the structure of the rotation-age behaviour suggests that our model-dependent age inference may in fact be reliable, since both are determined in different ways: rotation is deduced model independently from local mode-splitting observations, and age obtained from stellar-models fitted to spectroscopic parameters and whole seismic spectra.

SOFTWARE USED

1. Numpy (Harris et al. 2020)
2. Scipy (Virtanen et al. 2020)
3. Lightkurve (Collaboration & Cardoso 2018)
4. scikit-learn (Pedregosa et al. 2011)
5. matplotlib (Hunter 2007)
6. multiprocessing (McKerns et al. 2012)
7. pandas (McKinney et al. 2010)
8. astroquery (Ginsburg et al. 2019)

SUPPLEMENTARY MATERIALS

APPEDIX A: REMOVING EXTERNAL PERIODICITY

We first eliminated externally arising sources of periodicity from binary and multiple-star systems from our sample by cross-matching with the Washington Double Star (WDS) (Mason et al. (2020)) catalogue. This step was crucial

in preventing the introduction of additional frequencies or regular patterns due to extrinsic brightness variations and also to avoid misinterpreting modes.

Further, to decrease the possibility of false positives, we cross-matched our sample with the SIMBAD (Wenger et al. (2000)) database for the object types mentioned below and subsequently discarded them: Ellipsoidal Variable, Eclipsing Binary, Spectroscopic Binary, BY Dra Variable, Symbiotic Star, X-ray Binary, Low Mass X-ray Binary, High Mass X-ray Binary, Cataclysmic Binary, Classical Nova, Double or Multiple Star, RR Lyrae Variable, Cepheid Variable, Classical Cepheid Variable, beta Cep Variable, Evolved Supergiant, Red Supergiant, Yellow Supergiant, Blue Supergiant, Wolf-Rayet, Neutron Star, Pulsar, Red Giant Branch star, Hot Subdwarf, Carbon Star, S Star, Long-Period Variable, Mira Variable, OH/IR Star, Post-AGB Star, RV Tauri Variable, Planetary Nebula, White Dwarf, Low-mass Star, Brown Dwarf, Extra-solar Planet, Eruptive Variable, Rotating Variable, Irregular Variable, High Proper Motion Star, Cluster of Stars, Globular Cluster , Open Cluster, Association of Stars, Stellar Stream, Moving Group, Type II Cepheid Variable.

Finally, we calculated the Renormalized Unit Weight Error (RUWE) from GAIA-dr2 (Gaia Collaboration 2018, Gaia Collaboration et. al. 2018), and removed the stars with RUWE greater than 2.0, as it may indicate the presence of binary and multiple-star systems. It is derived by adjusting the Unit Weight Error (RUWE), a statistical measure of a star's goodness of fit to GAIA's five-parameter astrometric model, encompassing positions, parallaxes, and proper motions. A RUWE of 1.0 ideally characterizes a well-behaved single star. However, in practice, RUWE values often deviate due to extreme magnitudes and colors. To address this, RUWE is re-normalized through division by a reference RUWE value of a carefully chosen well-behaved star, whose magnitude and colour are stable. Stars with RUWE greater than 2.0 may indicate the presence of a binary or multiple-star system (Evans 2018). Thus, we removed stars with RUWE values greater than 2.0 from our sample.

APPENDIX B: ADDITIONAL FIGURES

Figure S1 shows the distribution of $\Delta\nu$ values for all the 436 regular δ Scuti Stars. The median value of $\Delta\nu$ for these stars is $6.66 d^{-1}$.

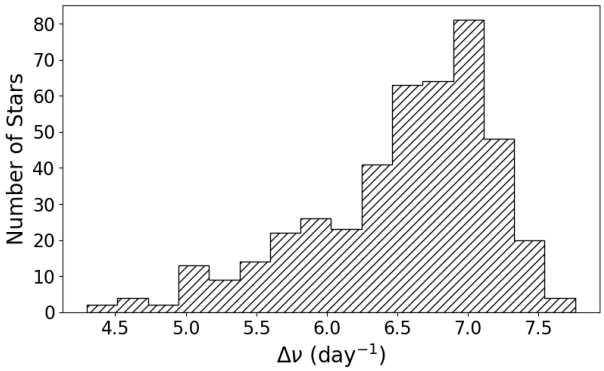

Figure S1: Distribution of $\Delta\nu$ of all the 436 δ Scutis exhibiting regular oscillation patterns.

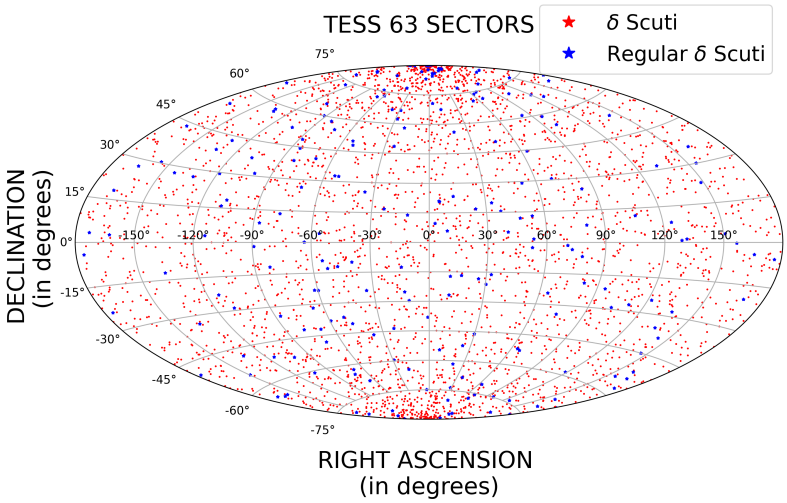

Figure S2: Sky map of δ Scutis from the first 63 sectors of TESS in right ascension and declination. The red dots represent all the δ Scutis and the blue dots represent regular pulsators.

In figure S3, we present several examples of regular δ Scutis with distinct vertical ridges. The ridge on the right corresponds to the $\ell = 0$ mode and the one on the left to the ℓ=1 mode.

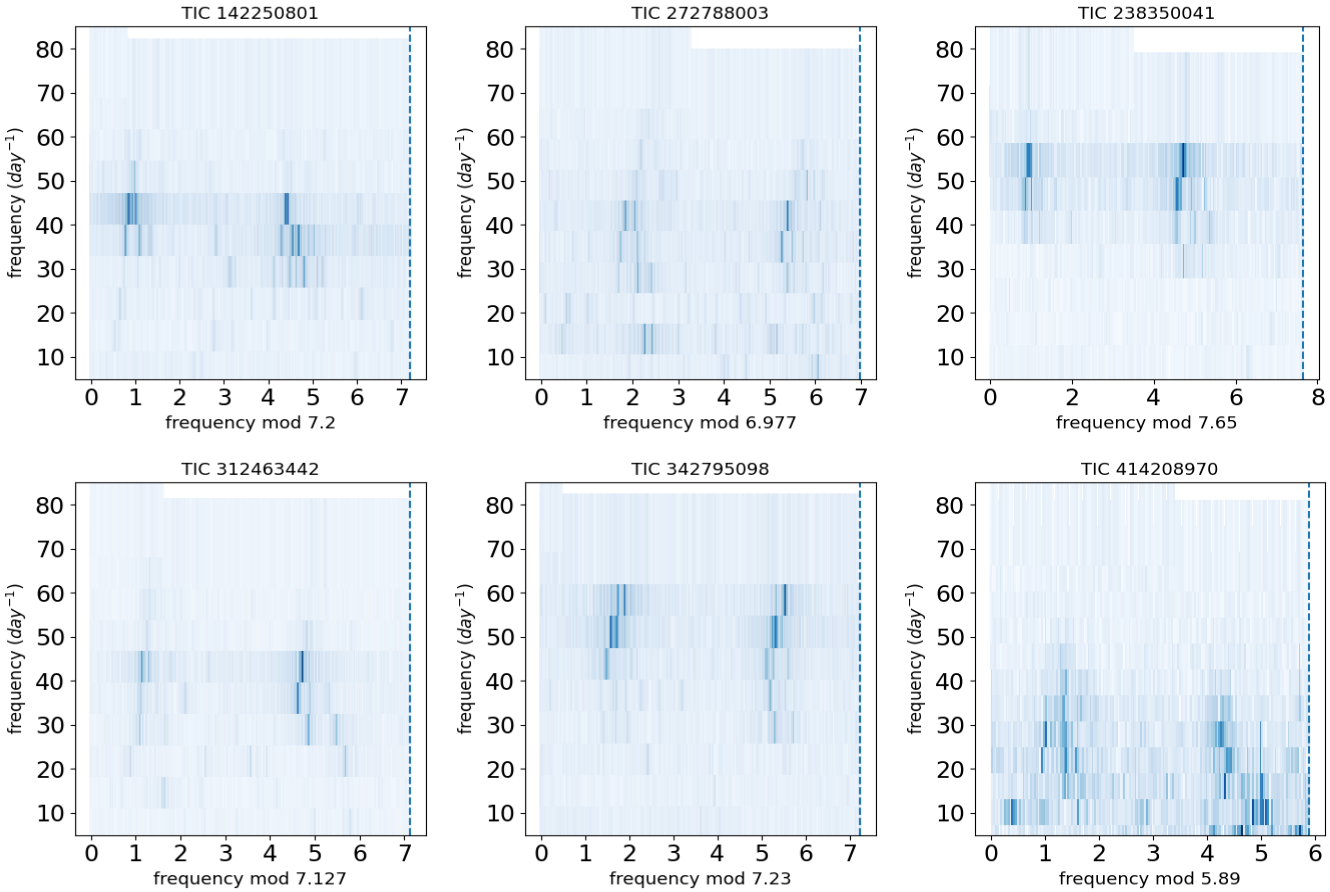

Figure S3: Échelle diagrams of δ Scutis exhibiting regular frequency separations in their oscillation spectra.

Figure S4 indicates that most regularly pulsating δ Scutis lie near the main sequence and stretch into the instability strip. The majority of them have effective temperatures ranging from 5000K to 10000K.

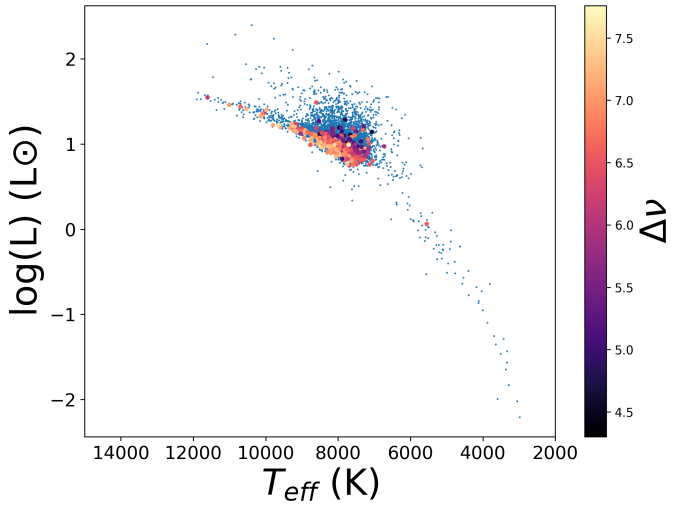

Figure S4: HR diagram of δ Scutis (blue dots) and regular pulsators (varying coloured dots) along with their $\Delta\nu$ values.

Figure S5 illustrates two examples from the sample, in which rotational splitting may be seen across all radial orders.

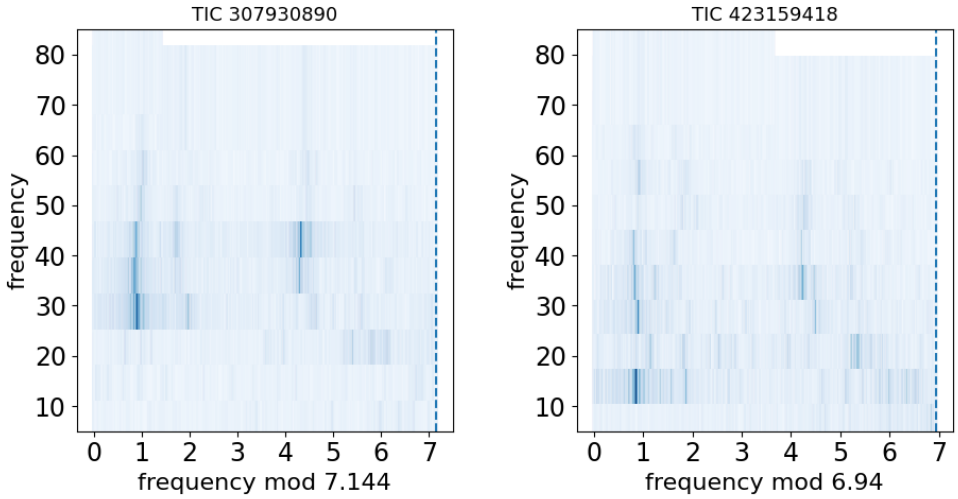

Figure S5: Échelle diagrams illustrating rotational splitting in dipole modes

We were able to obtain GAIA DR3 metallicities (described as `mh_gspphot`) for some stars in our sample. We compared their statistics against the distributions of our inferred metallicities, shown in figure S6. The former refers to surface metallicity, while the latter points to global metallicity. Surface and global metallicities of stars are expected to remain identical due to mixing processes, provided no significant mechanisms hinder this homogenization.

The following figure shows 3 cases of the auto-correlation algorithm introduced in section 2.3 to sort the stars in ascending order of their spectral regularity and simultaneously determine their large frequency separations ($\Delta\nu$).

APPENDIX D: TABLES

The table below contains 436 regularly pulsating δ Scuti stars along with their physical parameters.

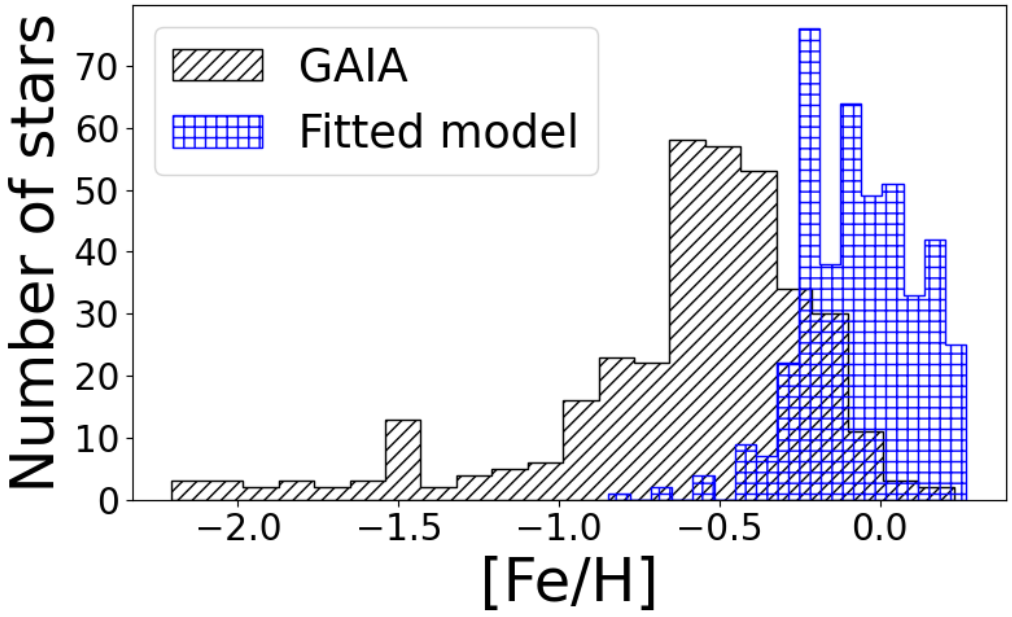

Figure S6: Comparison between distributions of [Fe/H] obtained from the fitted model (in blue checkers) and GAIA DR3 `mh_gspphot` (in black slanted lines). It appears that our inferences overestimate the metalicities of the examined stars. The reason is not straightforward to guess, however we presume while the Gaia provided [Fe/H] is spectroscopically measured from the atmospheric Fe abundance, our inference represents the initial global metalicity Z_i, although for the sake of comparison we obtained [Fe/H] using the simpler formula: $[\mathrm{Fe/H}] = \log_{10}(Z_i/Z_\odot)$. Regardless this discrepancy, both ours and Gaia data suggest that most of the values remain below the solar metalicity $Z_\odot$ (or [Fe/H]=0).

Table S1. Properties of regularly pulsating δ Scutis

TIC ID	$\Delta\nu$	M	Z	τ	$\chi^2_{\min}$	confidence
	day^{-1}	$M_\odot$		Myr		
148933	5.899 ± 0.174	$1.680 \pm (0.110)$	$0.010 \pm (0.0056)$	$8.050 \pm (2.149)$	0.00861	0.92606
1093492	6.273 ± 0.298	$1.620 \pm (0.079)$	$0.008 \pm (0.0046)$	$7.970 \pm (2.703)$	0.00851	0.92651
1260909	6.150 ± 0.271	$1.680 \pm (0.085)$	$0.014 \pm (0.0045)$	$10.790 \pm (2.044)$	0.00357	0.95235
4179118	6.326 ± 0.238	$1.800 \pm (0.064)$	$0.011 \pm (0.0044)$	$555.130 \pm (130.255)$	0.01361	0.90713
7209383	6.204 ± 0.230	$1.750 \pm (0.114)$	$0.016 \pm (0.0059)$	$11.220 \pm (2.545)$	0.00518	0.94263
7623467	7.125 ± 0.111	$1.640 \pm (0.062)$	$0.009 \pm (0.0043)$	$495.130 \pm (156.597)$	0.01007	0.92005
9591460	6.252 ± 0.349	$1.600 \pm (0.061)$	$0.014 \pm (0.0039)$	$12.500 \pm (3.117)$	0.00508	0.94316
9709684	6.650 ± 0.430	$1.550 \pm (0.063)$	$0.009 \pm (0.0037)$	$9.480 \pm (2.842)$	0.00536	0.94162
11227040	6.100 ± 0.320	$1.540 \pm (0.050)$	$0.014 \pm (0.0034)$	$803.160 \pm (210.081)$	0.00330	0.95416
12234050	6.444 ± 0.050	$1.520 \pm (0.068)$	$0.008 \pm (0.0039)$	$9.160 \pm (2.500)$	0.00157	0.96835
14172135	6.426 ± 0.328	$1.680 \pm (0.083)$	$0.018 \pm (0.0047)$	$14.190 \pm (2.373)$	0.00461	0.94588
14254276	7.242 ± 0.214	$1.640 \pm (0.064)$	$0.008 \pm (0.0040)$	$8.610 \pm (2.898)$	0.00598	0.93838
14435997	6.957 ± 0.121	$1.580 \pm (0.065)$	$0.015 \pm (0.0038)$	$15.030 \pm (2.782)$	0.00733	0.93179
15367231	6.840 ± 0.213	$1.680 \pm (0.088)$	$0.009 \pm (0.0049)$	$8.540 \pm (2.676)$	0.01026	0.91931
16698327	5.719 ± 0.183	$1.600 \pm (0.106)$	$0.011 \pm (0.0051)$	$9.100 \pm (1.409)$	0.01122	0.91563
17489989	6.478 ± 0.320	$1.620 \pm (0.065)$	$0.011 \pm (0.0040)$	$9.560 \pm (2.932)$	0.00571	0.93974
20378544	5.804 ± 0.228	$1.700 \pm (0.090)$	$0.014 \pm (0.0049)$	$8.680 \pm (2.154)$	0.00807	0.92842
20559588	7.207 ± 0.133	$1.580 \pm (0.054)$	$0.008 \pm (0.0036)$	$9.230 \pm (3.265)$	0.00445	0.94682
21702059	6.588 ± 0.267	$1.580 \pm (0.065)$	$0.012 \pm (0.0037)$	$12.110 \pm (2.738)$	0.00539	0.94145
22454293	5.208 ± 0.135	$1.800 \pm (0.098)$	$0.022 \pm (0.0049)$	$9.060 \pm (1.707)$	0.00374	0.95126

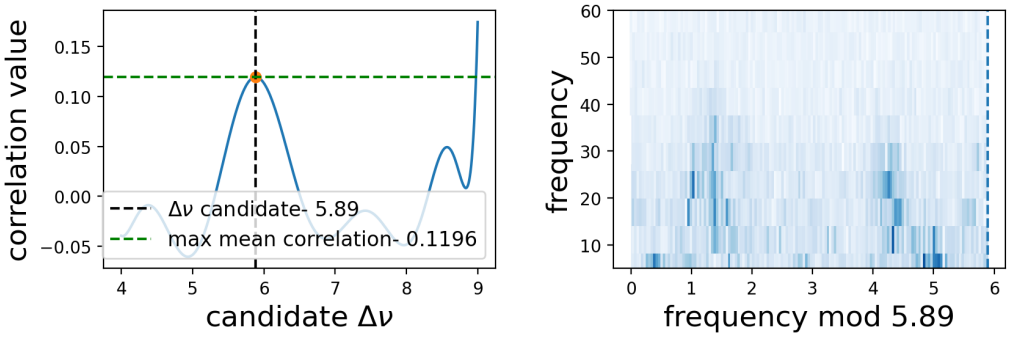

(i) Case A

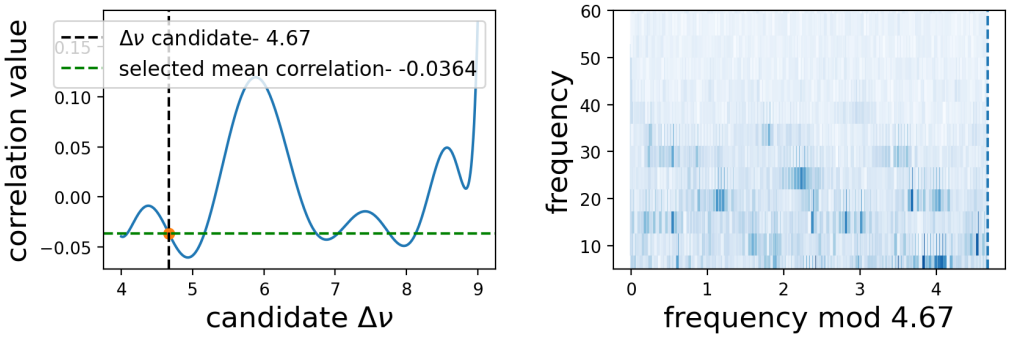

(ii) Case B

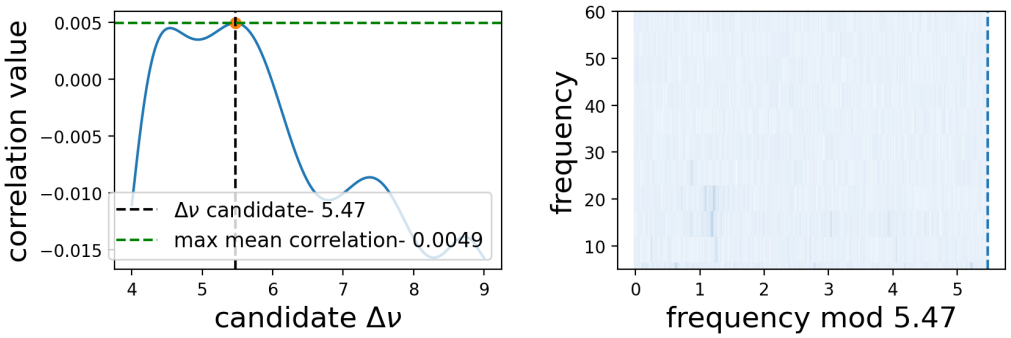

(iii) Case C

Figure S7: Case A displays the correlation graph of a regular star with the chosen candidate $\Delta\nu$ corresponding to the global maximum and the resulting Échelle diagram.
Case B displays the correlation graph of a regular star with the selected candidate $\Delta\nu$ corresponding to a lower correlation value and the resulting Échelle diagram.
Case C displays the correlation graph of an irregularly pulsating star with the selected candidate $\Delta\nu$ corresponding to the global maximum and the resulting Échelle diagram.

22734315	7.172 ± 0.291	$1.560 \pm (0.063)$	$0.010 \pm (0.0039)$	$12.360 \pm (2.869)$	0.00292	0.95687
22878162	6.560 ± 0.197	$1.600 \pm (0.064)$	$0.006 \pm (0.0035)$	$7.430 \pm (2.994)$	0.02544	0.87328
23732922	6.977 ± 0.233	$1.500 \pm (0.056)$	$0.008 \pm (0.0038)$	$711.030 \pm (217.926)$	0.00562	0.94023
24773594	6.937 ± 0.176	$1.700 \pm (0.076)$	$0.010 \pm (0.0045)$	$8.750 \pm (2.801)$	0.00668	0.93488
25801158	6.020 ± 0.158	$1.700 \pm (0.074)$	$0.015 \pm (0.0040)$	$10.350 \pm (2.359)$	0.00758	0.93060
25940862	5.005 ± 0.116	$1.640 \pm (0.075)$	$0.018 \pm (0.0041)$	$10.190 \pm (2.403)$	0.00725	0.93215
26633024	7.100 ± 0.222	$1.680 \pm (0.063)$	$0.014 \pm (0.0041)$	$348.840 \pm (182.256)$	0.01530	0.90155

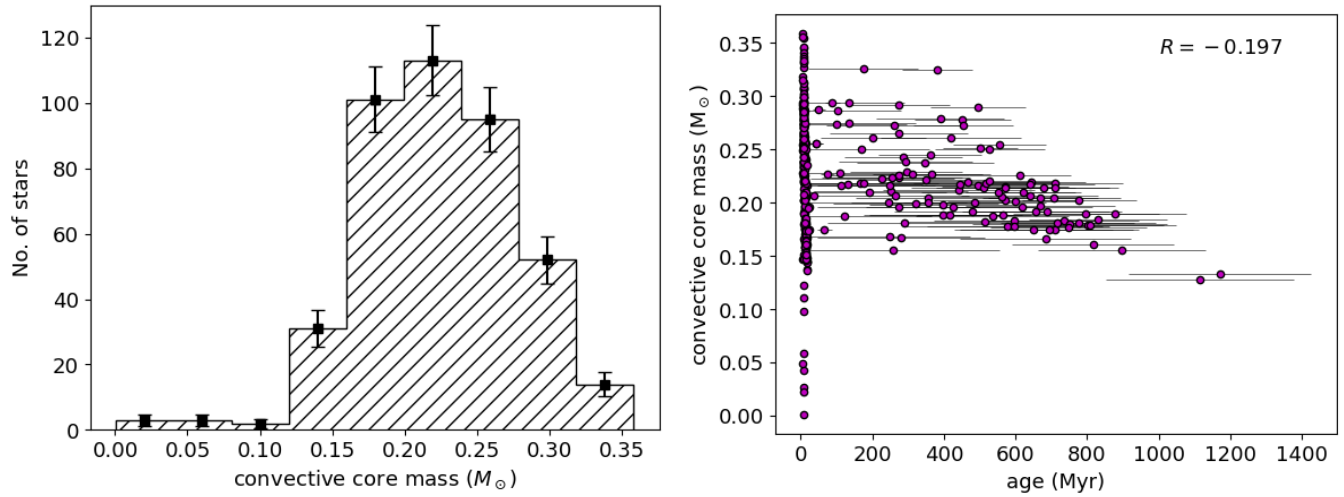

(a) (b)

Figure S8: (a) Distribution of convective core masses of the regularly oscillating δ Scuti stars. (b) Evolution of convective core masses with stellar ages, showing a declining correlation of Pearson $R = -0.197$. During main sequence evolution, cores of the stars shrink, thereby experiencing a mass loss. The correlation R turns out small due to the scattered presence of very young stars, ignoring which R coefficient raises to -0.521.

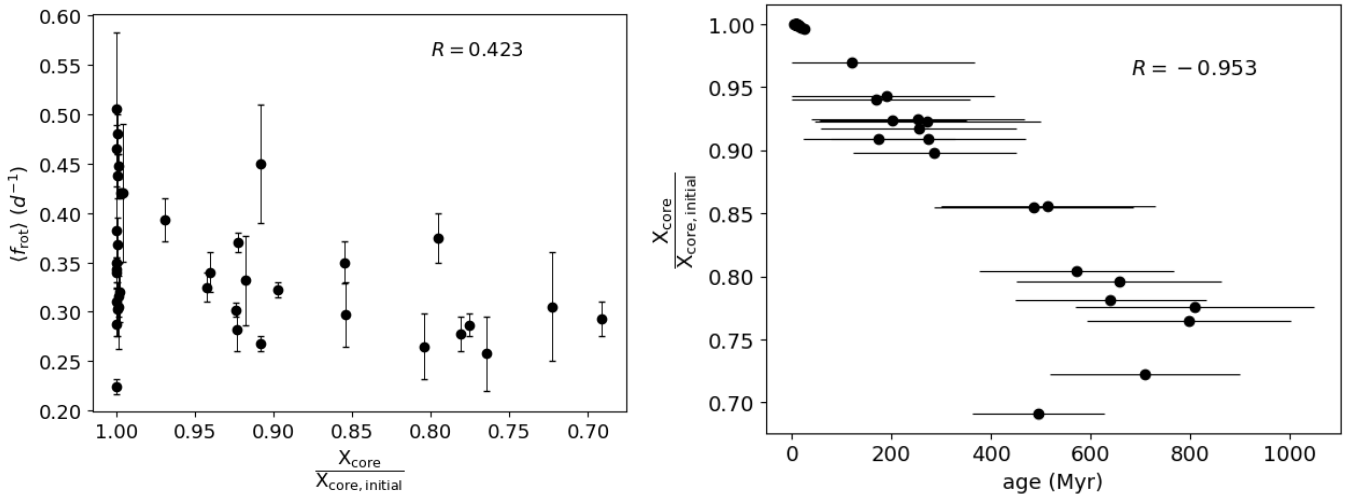

(a) (b)

Figure S9: (a) Average envelope rotation as a function of core Hydrogen content X_c (normalized by the initial value $X_{c,i}$) of the 38 stars that show rotational splitting. Normalized core Hydrogen content serves as the most reliable representation of the phase of stellar evolution, The correlation coefficient R of 0.423 between two quantities implies that the dependence is likely not spurious. The correlation is diminished by the cluster of the youngest stars at the left. (b) Evolution of core Hydrogen abundances of the same stars with their ages. The strong anti-correlation with $R = -0.953$ delineates the tight dependence of core Hydrogen abundance over stellar ages, the former linearly declining while the latter advances.

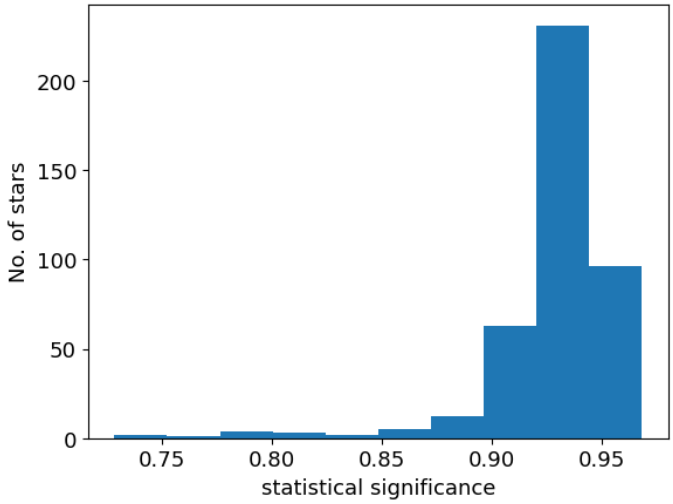

Figure S10: Distribution of statistical significance of the best fit stellar models for the 436 δ Scuti stars showing regular frequency oscillation. The best fit models were obtained by χ^2 minimization between the observables and model characteristics (section 2.4).

.

.

Table S1. The table contains the TIC IDs of regularly pulsating stars and their parameters $\Delta\nu$, mass, Z and age along with their uncertainties. Values within parentheses represent the uncertainties, obtained from the projections of the 1σ error ellipses onto the corresponding variable dimension, thus retaining their complete inter-parametric correlation. The last coulmn carries the $\chi^2_{\rm min}$ values corresponding to the best fitted stellar model identified using equation 2. The closer they are to 0, the better the fit. The remaining data are available in the online version of this paper.

The following table lists the TIC IDs, their large frequency separation, and their rotational frequencies for the 38 δ Scuti stars with clear rotational splittings.

Table S2. Rotational rates derived from rotational splittings

TIC ID	$\Delta\nu$ day^{-1}	$f_{\rm rot}$ day^{-1}
14172135	6.430 ± 0.330	0.240 ± 0.050
30624832	6.660 ± 0.220	0.350 ± 0.030
39669647	7.210 ± 0.200	0.390 ± 0.050
42827654	7.060 ± 0.540	0.320 ± 0.010
44540850	7.160 ± 0.100	0.380 ± 0.040
59365685	6.730 ± 0.250	0.380 ± 0.070
65734585	6.890 ± 0.300	0.500 ± 0.050
72399358	5.220 ± 0.190	0.540 ± 0.040
111840813	6.580 ± 0.320	0.330 ± 0.050
117229176	6.880 ± 0.260	0.360 ± 0.070
130646525	6.730 ± 0.220	0.280 ± 0.010
136795223	7.380 ± 0.210	0.400 ± 0.100
165674519	6.630 ± 0.330	0.310 ± 0.060

168002821	5.670 ± 0.480	0.280 ± 0.010
169464993	7.200 ± 0.260	0.430 ± 0.070
175022647	6.910 ± 0.170	0.260 ± 0.030
177715827	7.500 ± 0.230	0.440 ± 0.040
216904777	6.200 ± 0.430	0.350 ± 0.000
232729333	5.900 ± 0.300	0.470 ± 0.010
235297990	7.390 ± 0.460	0.240 ± 0.030
238641255	7.170 ± 0.290	0.480 ± 0.110
244920200	6.060 ± 0.290	0.310 ± 0.030
253151478	6.820 ± 0.330	0.270 ± 0.030
255589897	6.750 ± 0.700	0.220 ± 0.010
259931869	6.880 ± 0.360	0.450 ± 0.140
279019299	6.800 ± 0.200	0.600 ± 0.050
282742134	7.040 ± 0.300	0.430 ± 0.050
307930890	7.210 ± 0.270	0.490 ± 0.050
323290266	6.920 ± 0.220	0.360 ± 0.040
324515520	6.350 ± 0.190	0.450 ± 0.110
351744075	7.500 ± 0.200	0.490 ± 0.070
365852391	6.870 ± 0.210	0.230 ± 0.020
377257563	5.910 ± 0.370	0.440 ± 0.010
405483817	6.980 ± 0.230	0.340 ± 0.030
408165734	6.860 ± 0.100	0.300 ± 0.050
423159418	6.840 ± 0.270	0.460 ± 0.040
445020995	6.020 ± 0.240	0.210 ± 0.070
458689740	6.310 ± 0.230	0.230 ± 0.020

Table S2. The table contains TIC IDs, large frequency spacings, and rotational frequencies of 38 δ Scuti stars.

APPENDIX E: OSCILLATION SPECTRA AND ÉCHELLE DIAGRAMS

We show Échelle diagrams and power spectra for 10 regularly pulsating δ Scuti stars. The complete collection of Échelle diagrams and their corresponding power spectra are made available in the online version of this paper.

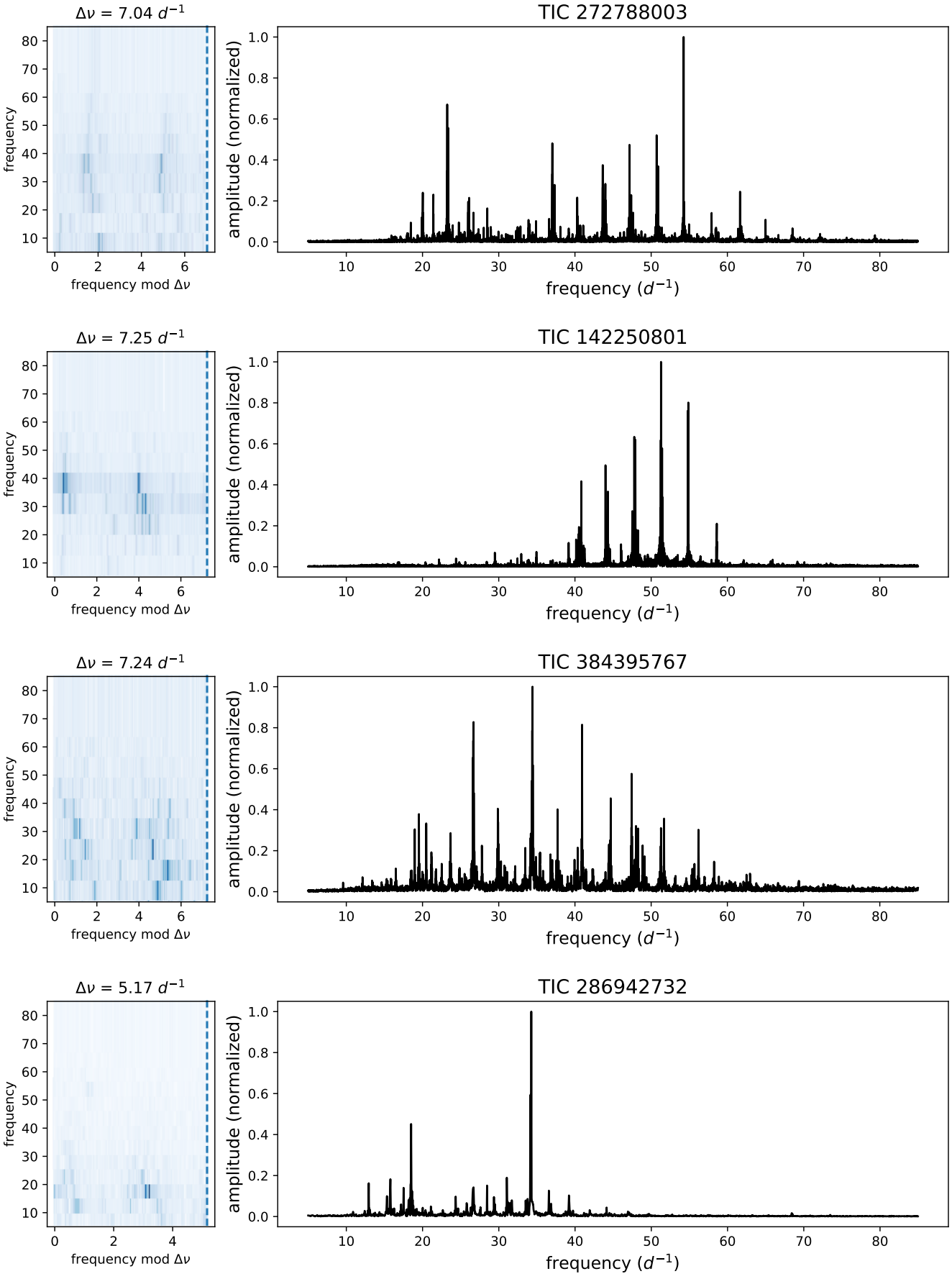
Δν = 7.04 d^{-1}
TIC 272788003
Δν = 7.25 d^{-1}
TIC 142250801
Δν = 7.24 d^{-1}
TIC 384395767
Δν = 5.17 d^{-1}
TIC 286942732
frequency
frequency mod Δν
amplitude (normalized)
frequency (d^{-1})

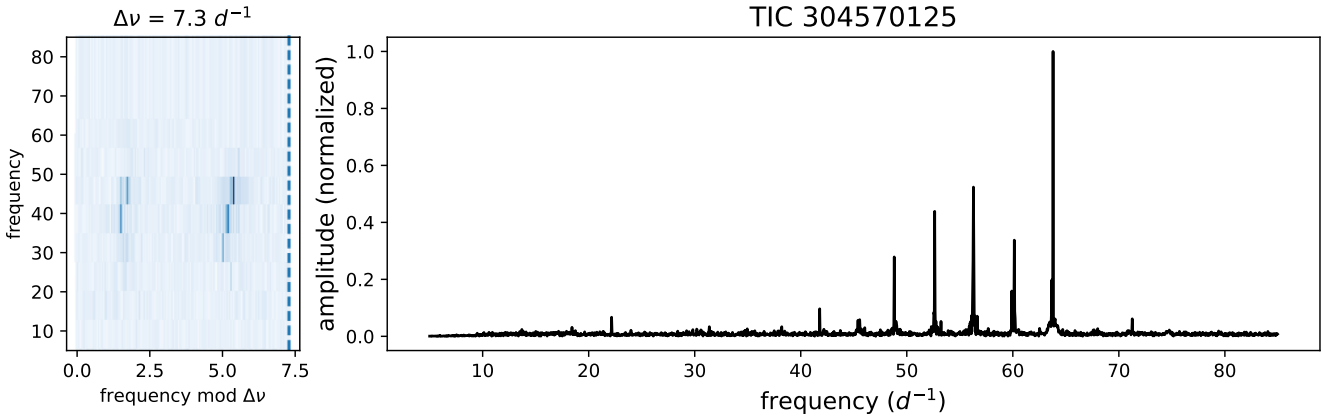
Δν = 7.3 d^{-1}
TIC 304570125
frequency
frequency mod Δν
amplitude (normalized)
frequency (d^{-1})

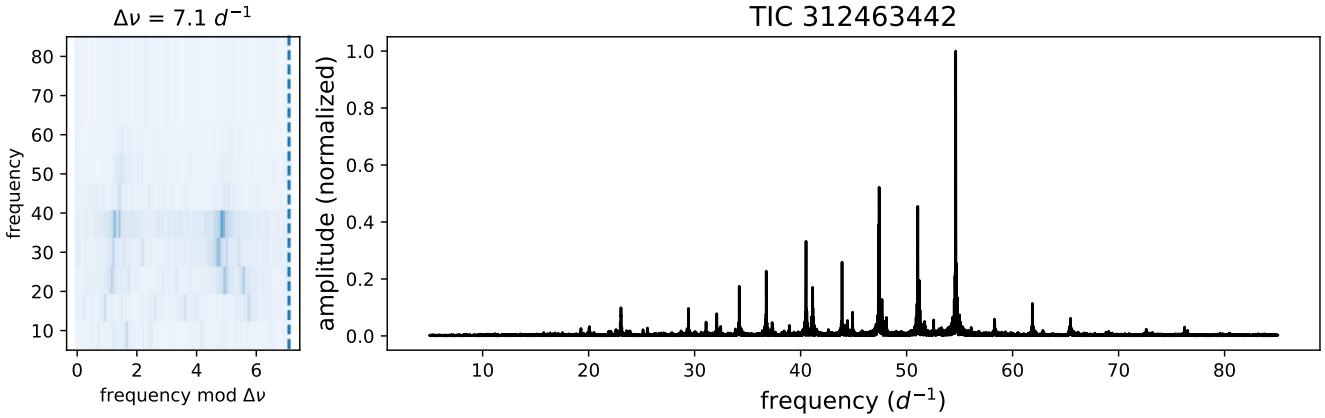
Δν = 7.1 d^{-1}
TIC 312463442
frequency
frequency mod Δν
amplitude (normalized)
frequency (d^{-1})

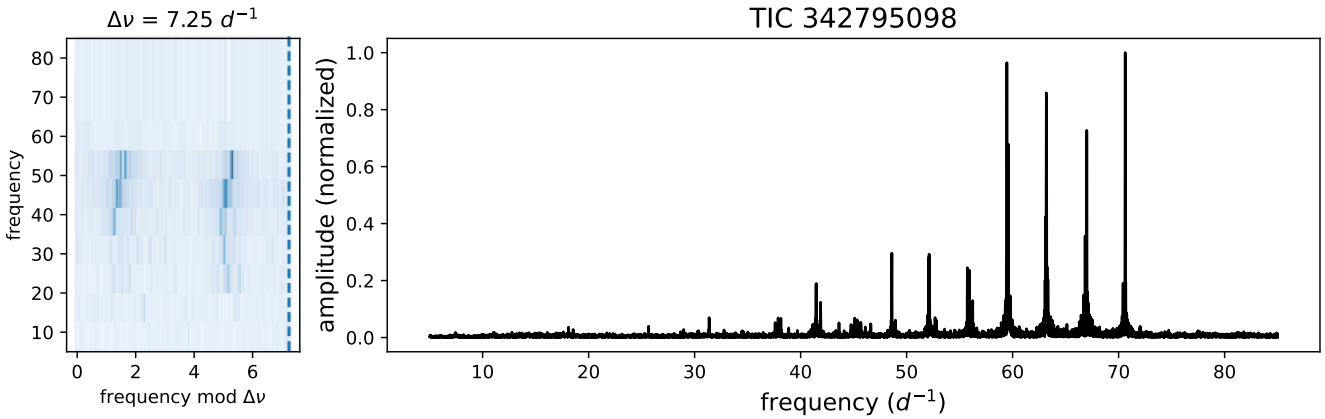
Δν = 7.25 d^{-1}
TIC 342795098
frequency
frequency mod Δν
amplitude (normalized)
frequency (d^{-1})

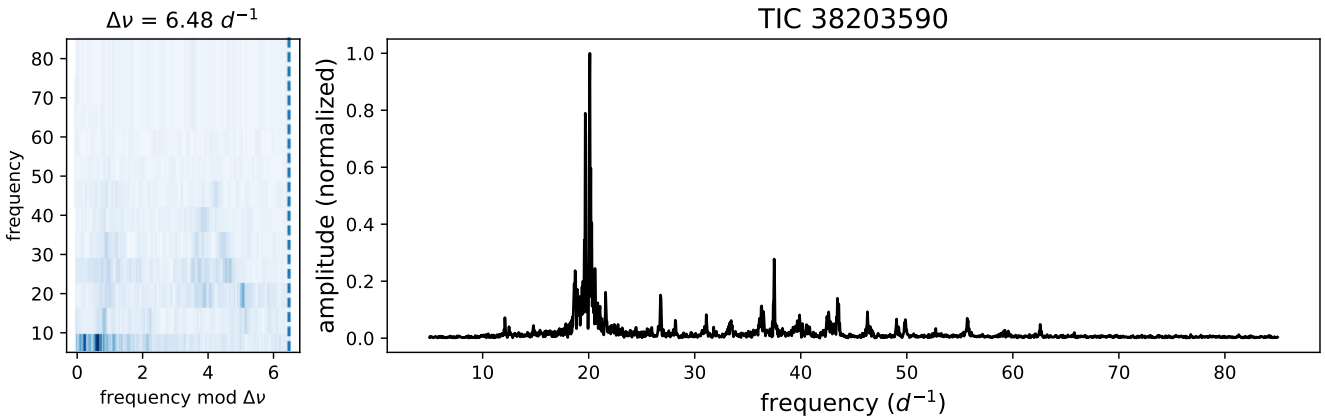
Δν = 6.48 d^{-1}
TIC 38203590
frequency
frequency mod Δν
amplitude (normalized)
frequency (d^{-1})

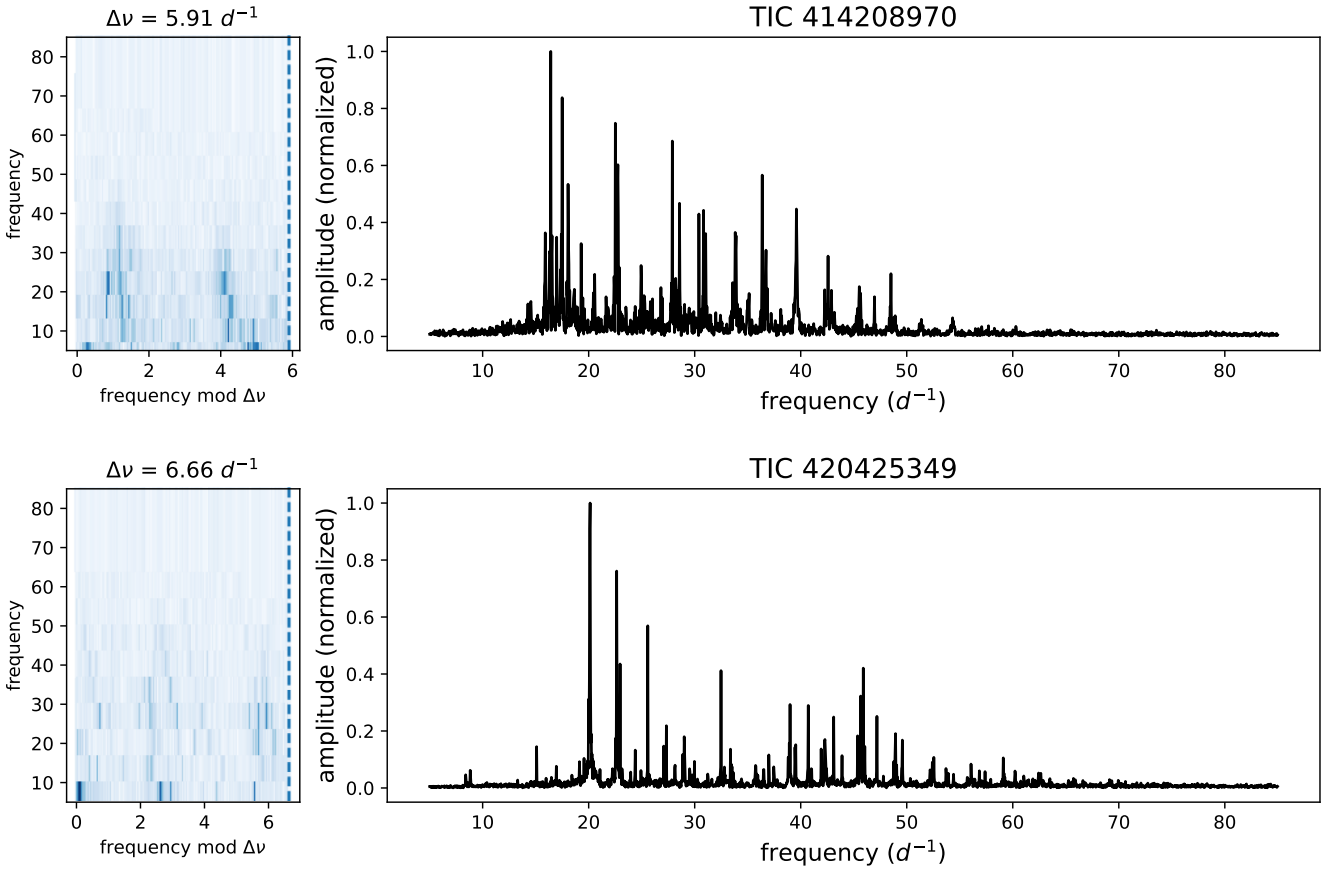

Figure S11: Échelle diagrams (left) and power spectra (right) of 10 regularly pulsating δ Scutis. The figures associated with the remaining stars are available as part of the extended supplementary material.

APPENDIX F: SUPPLEMENTARY RESOURCES

The following files are available as supplementary files with this article.

1. text file with TICIDs of 6711 δ Scuti stars.
2. text file containing M, Z, τ, and χ^2_{min} (with its statistical significance) like parameters for δ Scutis with regular oscillation.
3. pdf file with Échelle diagrams and power spectra of δ Scutis with regular pulsation.
4. text file containing Ids of 38 δ Scutis with rotational splittings along with their rotation rates.
5. text file providing frequencies of rotationally split multiplets and corresponding Ledoux constants for the 38 stars.
6. pdf file showing zoomed-in view of rotationally split frequency multiplets of the 38 stars.

DATA AVAILABILITY

All data generated or analyzed during this study are included in this published article and its supplementary information files.

CODE AVAILABILITY

The code to generate correlation plots are available from the corresponding author on reasonable request.

COMPETING INTERESTS

The authors have neither competing nor conflict of interests.

CORRESPONDENCE

All correspondence can be made with the leading author of the article.

REFERENCES

Aerts, C., Christensen-Dalsgaard, J., & Kurtz, D. W. 2010, Asteroseismology, doi: 10.1007/978-1-4020-5803-5

Ahlers, J. P., Barnes, J. W., & Myers, S. A. 2019, The Astronomical Journal, 158, 88, doi: 10.3847/1538-3881/ab27c4

Amard, L., & Matt, S. P. 2023, A&A, 678, A7, doi: 10.1051/0004-6361/202346148

Baglin, A., Auvergne, M., Barge, P., et al. 2009, 253, 71, doi: 10.1017/S1743921308026252

Barac, N., Bedding, T. R., Murphy, S. J., & Hey, D. R. 2022, Monthly Notices of the Royal Astronomical Society, 516, 2080, doi: 10.1093/mnras/stac2132

Barnes, S. A. 2003, ApJ, 586, 464, doi: 10.1086/367639

—. 2007, ApJ, 669, 1167, doi: 10.1086/519295

Bazot, M., Benomar, O., Christensen-Dalsgaard, J., et al. 2019, A&A, 623, A125, doi: 10.1051/0004-6361/201834594

Bedding, T. R., Murphy, S. J., et al. 2020, Nature, 581, 147, doi: 10.1038/s41586-020-2226-8

Bedding, T. R., Murphy, S. J., Crawford, C., et al. 2023, ApJL, 946, L10, doi: 10.3847/2041-8213/acc17a

Benomar, O., Takata, M., Shibahashi, H., Ceillier, T., & García, R. A. 2015, Monthly Notices of the Royal Astronomical Society, 452, 2654, doi: 10.1093/mnras/stv1493

Benomar, O., Bazot, M., Nielsen, M. B., et al. 2018, Science, 361, 1231–1234, doi: 10.1126/science.aao6571

Bishop, C. M. 2006, Pattern Recognition and Machine Learning (Springer)

Borucki, W. J., Koch, D., Basri, G., et al. 2010, Science, 327, 977, doi: 10.1126/science.1185402

Bowman, D. M. 2020, Frontiers in Astronomy and Space Sciences, 7, doi: 10.3389/fspas.2020.578584

Braithwaite, J., & Spruit, H. C. 2004, Nature, 431, 819, doi: 10.1038/nature02934

Breger, M. 2000, in Astronomical Society of the Pacific Conference Series, Vol. 210, Delta Scuti and Related Stars, ed. M. Breger & M. Montgomery, 3

Breger, M., Balona, L., Lenz, P., et al. 2011, MNRAS, 414, 1721, doi: 10.1111/j.1365-2966.2011.18508.x

Briquet, M., Morel, T., Thoul, A., et al. 2007, Monthly Notices of the Royal Astronomical Society, 381, 1482, doi: 10.1111/j.1365-2966.2007.12142.x

Chevalier, C. 1971, A&A, 14, 24

Collaboration, L., & Cardoso. 2018, Lightkurve: Kepler and TESS time series analysis in Python, Astrophysics Source Code Library. http://ascl.net/1812.013

Collier Cameron, A., Davidson, V. A., Hebb, L., et al. 2009, Monthly Notices of the Royal Astronomical Society, 400, 451, doi: 10.1111/j.1365-2966.2009.15476.x

Deheuvels, S., García, R. A., Chaplin, W. J., et al. 2012, The Astrophysical Journal, 756, 19, doi: 10.1088/0004-637X/756/1/19

Deupree, R. G. 2011, The Astrophysical Journal, 742, 9, doi: 10.1088/0004-637X/742/1/9

Dupret, M.-A., Belkacem, K., Samadi, R., et al. 2009, A&A, 506, 57, doi: 10.1051/0004-6361/200911713

Evans, D. F. 2018, Research Notes of the AAS, 2, 20, doi: 10.3847/2515-5172/aac173

Fox Machado, L., Pérez Hernández, F., Suárez, J. C., Michel, E., & Lebreton, Y. 2006, A&A, 446, 611, doi: 10.1051/0004-6361:20053791

Fuller, J., Lecoanet, D., Cantiello, M., & Brown, B. 2014, The Astrophysical Journal, 796, 17, doi: 10.1088/0004-637X/796/1/17

Gaia Collaboration. 2018, VizieR Online Data Catalog, I/345

Gaia Collaboration et. al. . 2018, A&A, 616, A1, doi: 10.1051/0004-6361/201833051

García, R. A., & Ballot, J. 2019, Living Reviews in Solar Physics, 16, doi: 10.1007/s41116-019-0020-1

García Hernández, A., Moya, A., Michel, E., et al. 2009, A&A, 506, 79, doi: 10.1051/0004-6361/200911932

Ginsburg, A., Sipőcz, B. M., Brasseur, C. E., et al. 2019, AJ, 157, 98, doi: 10.3847/1538-3881/aafc33

Guzik, J. A. 2021, Frontiers in Astronomy and Space Sciences, 8, 55, doi: 10.3389/fspas.2021.653558

Handler, G., Guzik, J. A., & Bradley, P. A. 2009, doi: 10.1063/1.3246528

Harris, C. R., Millman, K. J., van der Walt, S. J., et al. 2020, Nature, 585, 357, doi: 10.1038/s41586-020-2649-2

Hartman, J. D., Gaudi, B. S., Pinsonneault, M. H., et al. 2009, The Astrophysical Journal, 691, 342, doi: 10.1088/0004-637X/691/1/342

Hunter, J. D. 2007, Computing in Science & Engineering, 9, 90, doi: 10.1109/MCSE.2007.55

Keszthelyi, Z., Meynet, G., Shultz, M. E., et al. 2020, Monthly Notices of the Royal Astronomical Society, 493, 518, doi: 10.1093/mnras/staa237

Kurtz, D. W., Saio, H., Takata, M., et al. 2014, Monthly Notices of the Royal Astronomical Society, 444, 102, doi: 10.1093/mnras/stu1329

Ledoux, P. 1951, ApJ, 114, 373, doi: 10.1086/145477

Li, G., Van Reeth, T., Bedding, T. R., et al. 2019, Monthly Notices of the Royal Astronomical Society, 491, 3586, doi: 10.1093/mnras/stz2906

Li, T., Li, Y., Bi, S., et al. 2022, The Astrophysical Journal, 927, 167, doi: 10.3847/1538-4357/ac4fbf

Lomb, N. R. 1976, Astrophysics and Space Science, 39, 447, doi: 10.1007/BF00648343

Mamajek, E. E., & Hillenbrand, L. A. 2008, ApJ, 687, 1264, doi: 10.1086/591785

Mason, B. D., Wycoff, G. L., Hartkopf, W. I., Douglass, G. G., & Worley, C. E. 2020, VizieR Online Data Catalog, B/wds

Matthews, J. M. 2007, Communications in Asteroseismology, 150, 333, doi: 10.1553/cia150s333

Matthews, J. M., Kuschnig, R., Guenther, D. B., et al. 2004, Nature, 430, 51, doi: 10.1038/nature02671

McKerns, M. M., Strand, L., Sullivan, T., Fang, A., & Aivazis, M. A. G. 2012, Building a Framework for Predictive Science. https://arxiv.org/abs/1202.1056

McKinney, W., et al. 2010, in Proceedings of the 9th Python in Science Conference, Vol. 445, Austin, TX, 51–56

McQuillan, A., Mazeh, T., & Aigrain, S. 2014, ApJS, 211, 24, doi: 10.1088/0067-0049/211/2/24

Meibom, S., Mathieu, R. D., & Stassun, K. G. 2009, The Astrophysical Journal, 695, 679, doi: 10.1088/0004-637X/695/1/679

Murphy, S. J., Bedding, T. R., Gautam, A., & Joyce, M. 2023, A grid of 200,000 models of young δ Scuti stars using MESA and GYRE. https://arxiv.org/abs/2306.13142

Murphy, S. J., Bedding, T. R., White, T. R., et al. 2022, Monthly Notices of the Royal Astronomical Society, 511, 5718, doi: 10.1093/mnras/stac240

Murphy, S. J., Fossati, L., Bedding, T. R., et al. 2016, Monthly Notices of the Royal Astronomical Society, 459, 1201, doi: 10.1093/mnras/stw705

Murphy, S. J., Hey, D., Van Reeth, T., & Bedding, T. R. 2019, MNRAS, 485, 2380, doi: 10.1093/mnras/stz590

Murphy, S. J., Joyce, M., Bedding, T. R., White, T. R., & Kama, M. 2021, Monthly Notices of the Royal Astronomical Society, 502, 1633, doi: 10.1093/mnras/stab144

Murphy, S. J., Paunzen, E., Bedding, T. R., Walczak, P., & Huber, D. 2020, Monthly Notices of the Royal Astronomical Society, 495, 1888, doi: 10.1093/mnras/staa1271

Neiner, C., & Lampens, P. 2015, Monthly Notices of the Royal Astronomical Society: Letters, 454, L86, doi: 10.1093/mnrasl/slv130

Neiner, C., Wade, G. A., & Sikora, J. 2017, Monthly Notices of the Royal Astronomical Society: Letters, 468, L46, doi: 10.1093/mnrasl/slx023

Ochsenbein, F., Bauer, P., & Marcout, J. 2000, A&AS, 143, 23, doi: 10.1051/aas:2000169

Pamyatnykh, A. A., Handler, G., & Dziembowski, W. A. 2004, Monthly Notices of the Royal Astronomical Society, 350, 1022, doi: 10.1111/j.1365-2966.2004.07721.x

Paparó, M., Bognár, Zs., Benk"o, J. M., et al. 2013, A&A, 557, A27, doi: 10.1051/0004-6361/201321792

Paparó, M., Benkő, J. M., Hareter, M., & Guzik, J. A. 2016, The Astrophysical Journal Supplement Series, 224, 41, doi: 10.3847/0067-0049/224/2/41

Pedersen, M. G. 2022a, The Astrophysical Journal, 930, 94, doi: 10.3847/1538-4357/ac5b05

—. 2022b, The Astrophysical Journal, 940, 49, doi: 10.3847/1538-4357/ac947f

Pedregosa, F., Varoquaux, G., Gramfort, A., et al. 2011, Journal of Machine Learning Research, 12, 2825

Radick, R. R., Thompson, D. T., Lockwood, G. W., Duncan, D. K., & Baggett, W. E. 1987, ApJ, 321, 459, doi: 10.1086/165645

Reese, D., Ligniè res, F., & Rieutord, M. 2008, Astronomy & Astrophysics, 481, 449, doi: 10.1051/0004-6361:20078075

Reese, D. R., MacGregor, K. B., Jackson, S., Skumanich, A., & Metcalfe, T. S. 2009, A&A, 506, 189, doi: 10.1051/0004-6361/200811510

Reeth, T. V., Tkachenko, A., Aerts, C., et al. 2015, The Astrophysical Journal Supplement Series, 218, 27, doi: 10.1088/0067-0049/218/2/27

Reinhold, Timo, & Gizon, Laurent. 2015, A&A, 583, A65, doi: 10.1051/0004-6361/201526216

Ricker, G. R., Winn, J. N., Vanderspek, R., et al. 2015, Journal of Astronomical Telescopes, Instruments, and Systems, 1, 014003, doi: 10.1117/1.JATIS.1.1.014003

Rogers, T. M. 2015, The Astrophysical Journal Letters, 815, L30, doi: 10.1088/2041-8205/815/2/L30

Royer, F., Grenier, S., Baylac, M.-O., Gómez, A. E., & Zorec, J. 2002, A&A, 393, 897, doi: 10.1051/0004-6361:20020943

Scargle, J. 1983, The Astrophysical Journal, 263, doi: 10.1086/160554

Schmid, V. S., Tkachenko, A., Aerts, C., et al. 2015, A&A, 584, A35, doi: 10.1051/0004-6361/201526945

Scutt, O. J., Murphy, S. J., Nielsen, M. B., et al. 2023, Asteroseismology of δ Scuti stars: emulating model grids using a neural network. https://arxiv.org/abs/2302.11025

Skumanich, A. 1972, ApJ, 171, 565, doi: 10.1086/151310

Soderblom, D. R., & Valenti, J. 2007, 211, 103.27

Southworth, J., Murphy, S. J., & Pavlovski, K. 2023, Monthly Notices of the Royal Astronomical Society: Letters, 520, L53, doi: 10.1093/mnrasl/slad004

Steindl, T., Zwintz, K., & Müllner, M. 2022, A&A, 664, A32, doi: 10.1051/0004-6361/202243242

Suárez, J. C., García Hernández, A., Moya, A., et al. 2014, A&A, 563, A7, doi: 10.1051/0004-6361/201322270

Suárez, J. C., Moya, A., Amado, P. J., et al. 2008, The Astrophysical Journal, 690, 1401, doi: 10.1088/0004-637X/690/2/1401

Suárez, J. C., Goupil, M. J., & Morel, P. 2006, A&A, 449, 673, doi: 10.1051/0004-6361:20054181

Ulrich, R. K. 1986, ApJL, 306, L37, doi: 10.1086/184700

Uytterhoeven, K., Moya, A., Grigahcène, A., et al. 2011, A&A, 534, A125, doi: 10.1051/0004-6361/201117368

Vidotto, A. A., Gregory, S. G., Jardine, M., et al. 2014, Monthly Notices of the Royal Astronomical Society, 441, 2361, doi: 10.1093/mnras/stu728

Virtanen, P., Gommers, R., Oliphant, T. E., et al. 2020, Nature Methods, 17, 261, doi: 10.1038/s41592-019-0686-2

Walker, G., Matthews, J., Kuschnig, R., et al. 2003, PASP, 115, 1023, doi: 10.1086/377358

Wenger, M., Ochsenbein, F., Egret, D., et al. 2000, A&AS, 143, 9, doi: 10.1051/aas:2000332

Ziaali, E., Bedding, T. R., Murphy, S. J., Van Reeth, T., & Hey, D. R. 2019, Monthly Notices of the Royal Astronomical Society, 486, 4348, doi: 10.1093/mnras/stz1110

Zima, W., Wright, D., Bentley, J., et al. 2006, A&A, 455, 235, doi: 10.1051/0004-6361:20064877

Zwintz, K., Neiner, C., Kochukhov, O., et al. 2020, A&A, 643, A110, doi: 10.1051/0004-6361/202038210

Zwintz, K., Lenz, P., Breger, M., et al. 2011, A&A, 533, A133, doi: 10.1051/0004-6361/201117272